

Lawrence Berkeley National Laboratory

Lawrence Berkeley National Laboratory

Title

NEUTRON FLUX DENSITY AND SECONDARY-PARTICLE ENERGY SPECTRA
AT THE 184-INCH SYNCHROCYCLOTRON MEDICAL FACILITY

Permalink

<https://escholarship.org/uc/item/20h590db>

Author

Smith, A.R.

Publication Date

1978-07-01

Peer reviewed

NEUTRON FLUX DENSITY AND SECONDARY-PARTICLE ENERGY SPECTRA
AT THE 184-INCH SYNCHROCYCLOTRON MEDICAL FACILITY

A. R. Smith,* W. Schimmerling,** A. M. Henson,*
L. L. Kanstein,*** J. B. McCaslin,* L. D. Stephens, *
R. H. Thomas,* J. Ozawa,** and F. W. Yeater***

*Engineering and Technical Services Division

**Biomedical Division

***Accelerator Division

Lawrence Berkeley Laboratory
University of California
Berkeley, California 94720

— NOTICE —

This report was prepared as an account of work sponsored by the United States Government. Neither the United States nor the United States Department of Energy, nor any of their employees, nor any of their contractors, subcontractors, or their employees, makes any warranty, express or implied, or assumes any legal liability or responsibility for the accuracy, completeness or usefulness of any information, apparatus, product or process disclosed, or represents that its use would not infringe privately owned rights.

Fig

CONTENTS

ABSTRACT	1
1.0 INTRODUCTION	3
2.0 THE BIOMEDICAL FACILITY OF THE 184-INCH SYNCHROCYCLOTRON	7
3.0 CALCULATION OF NEUTRON FIELDS FROM ALPHA-PARTICLE INTERACTIONS	9
3.1 Introduction	9
3.2 Physical Basis of the Calculation	11
3.3 Calculation of Neutron Production in the 184-Inch Cyclotron Medical Cave	20
4.0 EXPERIMENTAL MEASUREMENTS AND TECHNIQUE	25
4.1 Beam Line Configurations	25
4.2 Neutron Detectors	25
4.3 Beam Monitors	26
4.4 Experimental Measurements	28
4.5 Secondary-Particle Spectra and Absorbed Dose Calculations	33
5.0 SUMMARY AND CONCLUSIONS	39
REFERENCES	43
TABLES	47
FIGURE LEGENDS	55
FIGURES	59

ABSTRACT

Helium ions, with an energy of 920 MeV, produced by the 184-inch synchro-cyclotron of the Lawrence Berkeley Laboratory are now being used in a pilot series to determine their efficacy in the treatment of tumors of large volume. The techniques for production of the large uniform radiation fields required for these treatments involve the use of beam-limiting collimators and energy degraders. Interaction of the primary beam with these beam components produces secondary charged particles and neutrons.

The sources of neutron production in the beam transport system of the alpha-particle beam have been identified and their magnitudes have been determined. Measurements with activation detectors and pulse counters of differing energy responses have been used to determine secondary particle spectra at various locations on the patient table. These spectra are compared to a calculation of neutron production based on best estimates derived from published cross sections. Agreement between the calculated spectra and those derived from experimental measurements is obtained (at the 10 to 20% level) when the presence of charged particles is taken into account.

The absorbed dose in soft tissue is not very sensitive to the shape of the incident neutron energy spectrum, and the values obtained from unfolding the experimental measurements agree with the values obtained from the calculated spectra within the estimated uncertainty of $\pm 25\%$. These values are about 3×10^{-3} rad on the beam axis and about 1×10^{-3} rad at 20 cm or more from the beam axis, per rad deposited by the incident alpha-particle beam.

Estimates of upper limit dose to two critical organs, the lens of the eye and red bone marrow, are ~ 10 rad and ~ 1 rad, respectively, for a typical treatment plan. The absorbed dose to the lens of the eye is thus well below

the threshold value for cataractogenesis estimated for fission neutrons.

An upper limit for the risk of leukemia is estimated to be ~0.04%.

1.0 INTRODUCTION

The 184-inch synchrocyclotron of the Lawrence Berkeley Laboratory, which accelerates protons to 740 MeV, deuterons to 456 MeV, and helium ions to 920 MeV, has been used for radiotherapy for more than fifteen years. Most of this work consisted of pituitary gland irradiations in the successful treatment of Hodgkins disease (Lawrence and Tobias, 1965a, 1965b). The benefits from the use of heavier high-energy heavy ions, such as carbon, neon, and argon nuclei, in the treatment of various tumors (Tobias, 1973) have spurred the development of such beams at the Lawrence Berkeley Laboratory. The radiobiological experiments that are necessary for pretherapeutic evaluation of these beams are being performed at the Bevalac (Grunder, 1974; Grunder and Selph, 1977). However, pilot series are already underway at the 184-inch synchrocyclotron for the treatment of brain, eye, pancreas, and other tumors (Castro, 1976).

The production of large, uniform irradiation fields is necessary in this application. Following a suggestion by Koehler and his colleagues (Schneider et al., 1974), Crowe et al. designed a large field (up to 30-cm diameter) using scatterers and beam flattening devices (1975). In addition, the beam line has collimators and energy degraders to obtain the desired depth-dose characteristics. All these devices are sources of secondary particles, of which neutrons are the most penetrating and biologically effective. Thus, the beam shaping devices will be sources of patient exposure outside the area of treatment.

Two possibilities are of particular concern. First, in the treatment of brain and eye tumors, the lens of the eye of the patient will be very close to the edge of the charged particle radiation field. In this case

it would be important to ensure that the neutron dose to the lens of the eye was below the threshold for cataract induction. This threshold has been estimated at 75 to 100 rad for fission neutrons, which, although not completely consistent with all the biological effects noted in accident victims, appears consistent with data obtained from animal experiments (Ham, 1960; Upton, 1968).

Second, there will be a small but significant radiation dose to the red bone marrow which may induce leukemia in the patient. Recently, from a new analysis of the incidence of leukemia in the Hiroshima and Nagasaki survivors, Rossi and Kelllerer (1974) have suggested that an absorbed dose rate of 0.5 rad/yr to the red bone marrow will result in a risk of radiation induced leukemia comparable with the "natural" rate ($\sim 3 \times 10^{-5} \text{ yr}^{-1}$). While there is not yet general agreement with the magnitude of this risk estimate, the National Committee on Radiation Protection and Measurements (NCRP) is at the present time evaluating the available data on the incidence of leukemia due to neutron irradiation. The risk estimate of Rossi and Kelllerer might perhaps be considered to be an upper limit for irradiation by fission neutrons. While it is not clear that the induction of leukemia by fission spectrum neutrons is similar to that due to neutrons produced by high-energy alpha-particle interactions, it is prudent to ensure that the neutron radiation field is understood. Only then can a proper assessment of the risk/benefit aspects of a particular therapy configuration be made.

In principle, it is possible to calculate the secondary particle production from a knowledge of the relevant production cross sections, and use computer codes to determine the resultant radiation field after the complex series of interactions of the particles with the various elements of the beam transport system (see section 2.0). However, this calculation would be extremely

tedious, and not particularly accurate at the present time. As discussed in section 3.0, a survey of the literature indicates that the relevant secondary particle production cross sections are largely unknown. Accordingly, rather than embark on a comprehensive program to calculate the secondary radiation field, a simple theoretical model has been developed to estimate production using the few data available. Such a calculation, in order to be useful in a quantitative way, should similarly include charged particle production, and interactions of the secondaries. The principal thrust of the work reported here is empirical in that a series of fairly complete measurements of the radiation field were undertaken. Quite good agreement was obtained between these measurements and the theoretical model. The magnitude of the absorbed doses in soft tissue due to neutrons suggests that an extensive calculational project is not warranted at the present time.

A series of preliminary measurements were made by Smith and his colleagues (Smith, 1975; Kanstein et al., 1975). These measurements showed that the absorbed dose rate due to stray neutrons just outside the treatment radiation field was less than 1% of the dose rate in the field, and identified some of the main sources of secondary neutrons in the beam line. However, these early measurements were limited by insufficient beam time to acquire spectral information and explore the details of the configurations used for patient treatment. Accordingly, a new series of experiments was made to extend the earlier results and establish more precise upper limits for the dose that might be due to neutrons in a treatment. This work, which is reported here, was directed toward the following objectives:

1. identification of the major sources of secondary particles, in particular neutrons, in the beam transport system;
2. measurement of the source strength of these components for use in future design modifications;
3. determination of the neutron intensity and spectrum at locations on the patient treatment table in order to calculate the absorbed dose to tissues not under treatment;
4. comparison of the absorbed dose to the patient resulting from neutrons produced by irradiation of the patient with those neutrons produced along the beam transport system.

This report presents a detailed description of the experimental measurements, as well as an approximate method of calculating neutron production by alpha particles.

2.0 THE BIOMEDICAL FACILITY OF THE 184-INCH SYNCHROCYCLOTRON

Figure 1 shows a plan view of the accelerator facility. The internal alpha-particle beam is extracted from the cyclotron at 920 MeV and transported into the medical treatment area.

The main elements of the treatment room are shown in Figure 2. They are: a "first scatterer" used to spread out the beam, a second scatterer with an annular aperture used for beam flattening, two collimating beam pipes, and a variable water degrader which holds up to 40 cm of water and is used to adjust the residual range of the beam. In addition, a spiral ridge filter (Chamberlain, 1960) and a brass collimator may be inserted upstream of the second scatterer. The purpose of the ridge filter is to spread the stopping region of the alpha particles over a predetermined distance, which in the case of the present experiment was 8 cm of tissue. The minimum thickness of the spiral ridge filter reduces the maximum energy of the beam to 720 MeV.

After passing through the spiral ridge filter, the beam size is limited by two iron pipes, each about 1-m long. The first pipe (0.78-m long, 0.22-m inner diameter) begins 0.37 m downstream from the spiral ridge filter. The second pipe which is larger (1.42-m long, 0.28-m inner diameter) begins 1.22 m downstream from the filter. A lead collimator 7.6-cm thick and 12-cm inner diameter is placed in the downstream end of the iron pipe to limit beam size. A schematic diagram of the beam line elements is shown in Figure 3.

Immediately in front of the patient, the field is shaped for each treatment series by the use of a specially prepared collimator. This collimator is made of a low melting point (70°C) alloy known as "Lipowitz alloy" (Hodgman, 1959) (the commercial name is Cerrobend), which has a density of 9.7 g/cm³

and the composition: Bi (50%), Pb (26.7%), Sn (13.3%), and Cd (10%). A 30-cm diameter collimator with a central rectangular aperture, 7.6 cm x 18 cm and 7.6-cm thick, was used for the measurements described here.

To understand the description of the measurements reported here it will be convenient to have a coordinate system in which the detector positions are identified. The coordinate frame will be that used by the Biomedical group to specify treatment regions. This coordinate system is centered at beam height on the beam axis and is referred to the center of the patient positioner, also known as ISAH (Irradiation Stereotaxic Apparatus for Humans). The x axis of the system is positive to the right of an observer placed at the origin and looking into the beam. The y axis is positive upwards. The z axis coincides with the beam axis and is positive in the direction of motion of the beam. This coordinate system is shown in Figure 4 and will be used henceforth.

Table I summarizes the location of each of the beam elements. These may be identified in the photographs (Figures 5 and 6).

3.0 CALCULATION OF NEUTRON FIELDS FROM ALPHA-PARTICLE INTERACTIONS

3.1 Introduction

Any attempt to calculate neutron production by alpha particles in the presently considered therapeutic configuration is complicated by the following features:

1. The beam energy is variable, and there are two sources of variability. The first is the presence of the ridge filter (introduced to spread the Bragg peak), which causes the energy of the beam to be variable further downstream. The second is the fact that the alpha particles lose energy as they penetrate objects downstream of the ridge filter. Therefore, neutrons are produced by alpha particles of different energy at different depths for every incident beam energy.
2. The existence of multiple thick sources. In addition to the energy degradation mentioned above, the finite thickness sources will introduce a dependence of the solid angle on the depth of production (especially noticeable for the sources closest to the detector). They will also cause the detector to sample different parts of the angular distribution which correspond to different source depths due to the same finite geometry.
3. The existence of several thick sources will introduce beam broadening due to multiple scattering, and will result in a significant probability for the produced neutrons to be multiply scattered, absorbed, or suffer nuclear interactions leading to neutron cascades.

This type of problem is usually treated by Monte Carlo techniques or solutions of the transport equations. In the particular case of alpha par-

ticles, there is the additional difficulty that cross sections are known for only a few limited cases. To the authors' knowledge, there are no existing measurements of the doubly differential cross sections, $d^2\sigma/dE d\Omega$, for the process



where A_t is the target atomic weight and X is an unidentified residuum.

In principle, the features of this reaction can be related to the constituent nucleons of the alpha particle, characterized by the energy per nucleon. At the energies of interest ($\epsilon < 230$ MeV/u), measurements of the doubly differential cross sections have only been reported for the (presumably similar) proton production process. Even here, the literature on these experiments is limited to $\epsilon = 205$ MeV/u (Bailey, 1956; Deutsch, 1955) and $\epsilon = 400$ MeV/u (Gutbrod et al., 1976; Westfall et al., 1976). Bailey's results, furthermore, are integrated over 0° to 65° .

Gabriel et al. (1970) have attempted a calculation of neutron production based on Bertini's (1963) Monte Carlo code for intranuclear cascades. In these calculations, neutrons and protons are produced in almost equal numbers, and the results are greater than Bailey's by a factor of two or more.

Other studies of alpha-particle induced reactions have concentrated on $(\alpha, \alpha n)$ total cross sections (Church, 1972) and other studies based on the production of radioactive nuclei X in reaction (1) (Radin, 1970; Radin et al., 1974). Such studies, as well as measurements of elastic alpha-particle scattering, constitute the bulk of the literature and are not applicable to this work.

The reason for this scarcity of data has been discussed by Church (1972), who attributed it to the existence of only two accelerators in the world routinely used for the production of high-energy alpha-particle beams: the LBL 184-inch cyclotron and a similar machine at the NASA Space Radiation Effects Laboratory. To these must now be added the LBL Bevatron/Bevalac (Ghiorso et al., 1973), which has not operated long enough to generate a substantial body of data, and some other machines currently in the planning or construction stage (Grunder and Selph, 1977).

The purpose of the present calculation is limited to an ad hoc attempt to derive useful interpolation formulae in order to obtain an estimate of the neutron production to be expected in a very complicated configuration. In the remainder of this section we shall describe the heuristic reasoning used to adapt results published for proton and deuteron induced reactions to an approximate solution of this problem. Even in this extremely simplified approach, a computer calculation was necessary and will be described.

3.2 Physical Basis of the Calculation

3.2.1 Clarification of interactions

The nuclear reactions leading to production of a neutron in equation (1) (where X represents a group of undetected particles which may include more neutrons) will be grouped into three classes for the purposes of this discussion.

1. "Evaporation," representing the boiling-off of neutrons from an excited target nucleus, or residuum of such a nucleus. This type of reaction has been discussed recently by Bowman and Blann (1969). It is based on well-known statistical models of the nucleus. These reactions can be characterized by a nuclear temperature, and factors dependent on the nuclear

density level distribution. It should be noted that a single temperature may be inadequate to describe the process, especially for heavier nuclei where neutrons may be emitted by more than one excited remnant.

2. "Stripping," representing reactions where a neutron in the alpha particle continues with the same velocity, while the rest of the helium nucleus collides with the target. This reaction is, of course, familiar in the case of deuterons (Serber, 1947) where it is routinely used for the production of neutrons (Goebel and Miller, 1971). In the case of high-energy, heavier ions, this reaction is better known as "fragmentation," or, specifically, "projectile fragmentation." It is a direct reaction, occurring only for peripheral collisions between projectile and target, and can be expected to result in sharply forward peaked neutrons, distributed narrowly about ϵ .

3. "Knock-on" or "central" collisions which result in the emission of one or more neutrons by the target nucleus or by an intermediate compound state consisting of a mixture of target and projectile.

3.2.2 Evaporation neutrons

Deutsch (1955) concluded that protons below about 10 MeV are predominantly produced by alpha particles via an evaporation-type process. Bailey (1956) found that the evaporation of protons was well represented by:

$$\frac{d^2\sigma_E}{dE d\Omega} = \sigma_\Omega \frac{E-V}{T^2} \{\exp -(E-V)/T\} , \quad (2)$$

where T represents the "nuclear temperature" (in MeV), E is the proton energy (MeV), V is the effective coulomb barrier, and σ_Ω is a constant found to be equal to 149 mb/sr for aluminum. Bailey also concludes that, for light

targets, the number of neutrons is equal to the number of protons, and that equation (2), with $V = 0$, also is a good representation of the evaporative neutron production. In this case, however, the nuclear temperature was reported to be in disagreement with predictions based on the Le Couteur model, and should be viewed as a phenomenological parameter.

In order to use equation (2) to predict evaporation neutrons, it becomes necessary to decide on the dependence of σ_{Ω} and T on the target mass, A_t . The values of T reported by Bailey are 2.6 MeV for aluminum and 3.3 MeV for silver. This is a small variation. The aluminum value was used for all targets with $A_t \leq 27$, and the silver value was arbitrarily assigned to all targets with $A_t > 27$.

The constant σ_{Ω} , in equation (2), should be related to the total cross section, calculated geometrically (Saito, 1975; Karol, 1975) as:

$$\sigma_{TOT} = \pi r_0^2 (A_{\alpha}^{1/3} + A_t^{1/3})^2 . \quad (3)$$

In the case of aluminum, σ_{Ω} was somewhat larger than $\sigma_{TOT}/4\pi$, and $\sigma_{\Omega} = \sigma_{TOT}/4\pi$ in the case of silver. This is what would be expected if the only process occurring at low energies was evaporation. In the absence of a satisfactory explanation for the larger value for aluminum, the constant σ_{Ω} was taken to be $\sigma_{TOT}/4\pi$.

3.2.3 Stripping

Serber (1947) has given an intuitive discussion of deuteron stripping, and derived results for both a transparent and an opaque nucleus. We shall adapt the formulae for a "transparent" target, since they are simpler to

calculate and yield results that are not substantially different from those for an opaque nucleus in the present context. In Serber's calculation, the differential cross section $d\sigma/dE$ is obtained by calculating the probability that the neutron has a certain momentum in the center of mass (CM) of the deuteron. The angular distribution is due to the transverse projection of this momentum, taken as

$$P_1 = \sqrt{2MB_d/2}, \quad (4)$$

where B_d is taken as the binding energy of the deuteron and M is the mass of the neutron. The momentum (per nucleon) of the deuteron is given by:

$$P_0 = \sqrt{2ME_d/2}, \quad (5)$$

where E_d is the total energy of the deuteron. The angular distribution of the neutrons will be characterized by an angle

$$\theta_c = P_1/P_0, \quad (6)$$

which is characteristically narrow for deuterons due to the small value of the binding energy but will be broader for other nuclei.

Serber's result for the energy dependence of the cross section is (E = neutron energy):

$$P(E)dE = \frac{\sqrt{B_d E_d} dE}{\pi \{ (E - E_d/2)^2 + B_d E_d \}} \quad (7)$$

His result for the angular distribution is:

$$P(\theta)d\Omega = \left[\left(\frac{1}{2\pi} \right) \frac{\theta_0}{\frac{\theta_0^2}{2} + \theta^2} \right]^{3/2} d\Omega, \quad (8)$$

where:

$$\theta_0 = \sqrt{B_d/E_d} \left\{ 1 - \left(\frac{E_d}{8Mc^2} \right) \right\}. \quad (9)$$

In order to adapt these results to alpha particles, we make the following substitutions, which are within the spirit of Serber's calculation:

$\frac{B_d}{2} \rightarrow B$, the separation energy of the neutron in the alpha particle
(= 20.58 MeV).

$\frac{E_d}{2} \rightarrow \epsilon$, the alpha-particle energy per nucleon (MeV/u).

$P_1 \rightarrow \sqrt{2MB}$, the momentum of the neutron in the alpha particle (this corresponds to thinking of B as a Fermi energy and justifies the resulting neutrons appearing at energies greater than ϵ).

$P_0 \rightarrow \sqrt{2M\epsilon} \left\{ 1 + \frac{1}{4} \frac{\epsilon}{Mc^2} \right\} \sim \sqrt{2M\epsilon}$ since the relativistic correction is ~5% in the worst case. Then,

$$\theta_0 = \sqrt{B/\epsilon} \left(1 - \frac{1}{4} \frac{\epsilon}{Mc^2} \right). \quad (10)$$

It will be convenient to approximate equation (8) by a gaussian having the same full width at half maximum (FWHM) in order to derive a normalization

constant. For this purpose we rewrite equation (8) in the alternate form given by Serber:

$$P(\zeta) d\Omega \propto (1+\zeta^2)^{-3/2} d\Omega, \quad (11)$$

where $\zeta = \theta/\theta_0$, and the gaussian form is:

$$P(\zeta) d\Omega \approx \exp(-\theta^2/b^2) d\Omega, \quad (12)$$

where

$$b^2 = \frac{2^{2/3}-1}{\ln 2} \frac{B}{\epsilon} \left(1 - \frac{1}{4} \frac{\epsilon}{Mc^2}\right). \quad (13)$$

The stripping cross section then becomes:

$$\frac{d^2\sigma_s}{dE d\Omega} = K \cdot \frac{\sqrt{4B\epsilon} \exp(-\theta^2/b^2)}{\pi((E-\epsilon)^2 + 4B\epsilon)}. \quad (14)$$

The normalization constant K is obtained from the condition that the integral equal the total stripping cross section, σ_s :

$$K \left(\int_0^\infty \frac{\sqrt{4B\epsilon} dE}{\{(E-\epsilon)^2 + 4B\epsilon\}} \int_0^\pi e^{-\theta^2/b^2} d\Omega \right) = \sigma_s. \quad (15)$$

The integrals can be evaluated in a straightforward way to yield:

$$K = \frac{\sigma_s}{\left(\frac{\pi}{2} + \arctan \sqrt{\frac{\epsilon}{4B}}\right) b^2}, \quad (16)$$

where use has been made of the narrow angular distribution to evaluate the integral in equation (15).

To find σ_s we use the result given by Goebel and Miller (1971) for deuterons on beryllium at 60 MeV (30 MeV/u), and the fact that according to Serber (and as is intuitively obvious):

$$\sigma_s = \left(\frac{\pi}{2}\right) R_t R_d , \quad (17)$$

where $R_t = r_0 A_t^{1/3}$ and R_d are the radii of the target nucleus and the deuteron, respectively. Goebel and Miller's most probable value for beryllium is $\sigma_s = 300$ mb, which is larger than that obtained using equation (17), and we take

$$\sigma_s = (300) (A_t/9)^{1/3} . \quad (18)$$

3.2.4 Central collisions

In order to obtain an estimate of the cross sections for central collisions, we use as a point of departure the recent, careful measurements of Gutbrod et al. (1976) for the reaction:



These data are reproduced in Figure 7 for angles of 30° through 150° , in 30° intervals. At the forward angles, these authors caution that an unknown fraction of the higher energy protons may be due to projectile fragmentation. In order not to include these protons, and to have a suitable form for

interpolation of the data, exponentials were fitted (by eye) to the lower proton energy portion of the data, to give the form:

$$\frac{d^2\sigma_K}{dE d\Omega} = A_1 \exp\{-A_2(\theta)E_n\} , \quad (20)$$

where A_1 and $A_2(\theta)$ are to be determined. A plot of the slopes A_2 versus the angle θ showed that, to a good approximation, A_2 also increased exponentially with θ .

As shown in Figure 7, the exponential fits seem to extrapolate to the same ordinate and this constraint was incorporated by making $A_1 = 43.4$ mb/MeV sr for all angles. The physical reasons for this were not investigated. Also, all angles used in the concurrent experiment were less than 90° , so that only the data in the top three curves of Figure 7 are used, where this procedure seems reasonable.

The variation of the parameters in equation (20) with target mass and projectile energy is not known. A comparison with Bailey's results showed that the slope A_2 in equation (20) could best be obtained from the slope of Gutbrod's data if it was assumed that the slopes were inversely proportional to $(A_t)^{2/3}$. A comparison of data published by the same authors of neon incident on uranium, at 250 and 400 MeV/u, showed some dependence on the projectile momentum. This dependence was irreconcilable with the relationship of the slope for alphas and may be due to protons originating in the incident projectile. Therefore, the slopes were taken to be independent of ϵ and were calculated according to:

$$A_2(\theta) = 0.0078 \left(\frac{238.03}{A_t} \right)^{2/3} \exp(0.92\theta) . \quad (21)$$

Similarly, it was found that the results at 400 MeV/u could be transformed into those at 205 MeV/u if it was assumed that A_1 was directly proportional to $(A_t)^{2/3}$.

The description of the "knock-on" or central collision neutrons given by equation (20) extrapolates to a finite cross section at zero neutron energy (E_n). In order to avoid double counting of neutrons in the "evaporation" region, a smooth cutoff (gaussian) was applied to "knock-on" neutrons below 12.5 MeV, with a width (standard deviation of the gaussian form) of 3.5 MeV.

Figure 8 shows the result of calculating the evaporation and "knock-on" neutrons in this manner. The thick, full curve represents the trend of Bailey's data at $\epsilon = 205$ MeV/u (errors are typically 10%). The two curves calculated as described above are also shown and add to the full curve. The uppermost curve shows the results obtained by integrating the 400 MeV/u data as published, and averaging between 0° and 65° . It is possible to use equation (21) to find an "average" angle ($\bar{\theta}$) for Bailey's results. This angle turns out to be $\sim 5^\circ$, which is a reasonable result.

The spectra resulting from the estimates described above are shown in Figure 9 for the case of water, an incident energy of 185 MeV/u, and an angle of $\sim 14^\circ$ (corresponding to a detector at $\ell = 10$ cm in the present experiment). The three regions where the different processes are thought to predominate are clearly indicated. Also shown, for comparison, is the stripping cross section that would be expected for the case of deuterons at this angle.

3.3 Calculation of Neutron Production in the 184-Inch Cyclotron Medical Cave

The number of neutrons of energy E produced at a given angle θ , incident upon a 1-cm^2 detector subtending a solid angle $d\Omega$, due to a flux of $I(\epsilon')$ alpha particles, will be given by:

$$N(E) = I(\epsilon') (nz) d\Omega \sum_i (d^2\sigma_i/dE d\Omega) , \quad (22)$$

where nz is the number of target atoms per cm^2 . Methods for estimating the cross sections have been described in the previous section. This section describes the treatment of variations in the incident energy ϵ' , variations in the cross sections due to energy degradation $\epsilon(z)$ in the absorber, and the geometry of the concurrent experiment.

The following additional assumptions and approximations are made in the calculation.

1. The only sources that contribute significantly to neutron production in a plane containing the experimental origin of coordinates and perpendicular to the beam are: the lead collimator, the water column, and the Cerrobend collimator. A preliminary calculation including other sources showed that their contribution is negligible, as confirmed by the experiment.
2. There is no multiple scattering. Alpha particles interacting in the lead and water sources are independent. Alphas interacting in the Cerrobend enter at an energy that corresponds to the incident beam degraded by traversal of the water column.
3. Secondary interactions are only considered to the extent that the alpha particles are assumed to be attenuated with a mean free path cal-

culated using the cross section given in equation (3), and that produced neutrons are assumed to be attenuated with a mean free path given by the neutron-nucleus inelastic cross section. These cross sections have been measured in the energy range of interest and have been found to vary little with energy. They are calculated (Schimmerling et al., 1973a) according to:

$$\sigma_{inel} = 43.4 A_t^{0.719} (\text{mb}) \quad (23)$$

The path length of the neutrons in the downstream absorbers is calculated as the intersection of their trajectory with a right cylinder, coaxial with the beam, of length and cross sectional area equal to that of the object (water column, collimator, etc.).

4. The solid angle, as a function of distance to the production point, does not vary significantly over the cross section of the source, i.e., all sources are approximated by line targets coaxial with the beam, and the incident number of alphas is taken as the alpha particle flux per incident energy interval times the area intercepted by the source. This assumption may be questionable, especially for the nearest targets, but is dictated by the necessity of limiting the computation time to practical values.

5. Two assumptions were made with respect to the incident energy. The first was that the incident flux was uniformly distributed over the incident energy interval $150 \leq \epsilon' \leq 190$ MeV/u determined by the ridge filter. The second possibility considered was a linear dependence such that the product of flux and dE/dx (ionization chamber "dose") would be constant over the extended Bragg peak. This added detail resulted in only negligible variations of the final results.

6. In order to make the energy variation $\epsilon(z)$ of the alphas tractable, the range of alpha particles in each absorber was calculated and fitted to a power law of the type:

$$\epsilon = C_1 R^{C_2}, \quad (24)$$

where R is the residual range. The validity of this approximation has been confirmed experimentally at about the 5% level (Schimmerling *et al.*, 1973b).

The calculation proceeds by computing the following quantities at each depth Z_i (g/cm^2) (measured from the incident beam direction) in absorber i :

1. solid angle, per cm^2 detector, given by $1/r^2(Z_i)$, where $r(Z_i)$ is the distance from the detector to the layer of absorber at depth Z_i ;
2. energy of the alpha particles, given by

$$\begin{aligned} \epsilon &= C_1 (R - Z_i)^{C_2}, \quad Z_i \leq R, \\ &= 0, \quad Z_i > R, \end{aligned} \quad (25)$$

for $R = R(\epsilon')$, the residual range of incident alphas of energy ϵ' ;

3. the cross sections as a function of ϵ and the angle $\theta = \arctan(\ell/d_i)$, where ℓ is the z coordinate of the detector, and d_i is the measured distance to layer Z_i of source i ;

4. the attenuation of alpha particles in the depth Z_i ;

5. the attenuation of neutrons in the depth $(D_i \cdot \rho - Z_i)/\cos\theta$ (g/cm^2),

where D_i is the thickness of the absorber and ρ the density, as well as the attenuation of neutrons in the downstream absorbers.

The number of neutrons at each neutron energy E , produced between Z_i and $Z_i + dZ_i$, is then calculated according to equation (22) for incident alpha particles of energy between ϵ' and $\epsilon' + d\epsilon'$ for each source. Let this number of neutrons be $N_i(E, Z_i, \epsilon') dX_i d\epsilon'$. Then the total number of neutrons with energy E is obtained from

$$N(E) = \sum_i \int_{\epsilon_1'}^{\epsilon_2'} d\epsilon' \int_0^{R'} dZ_i N_i(E, Z_i, \epsilon'), \quad (26)$$

$$(R' = \min(R_0, D_i)),$$

where R_0 is the residual range of the alpha particles having energy ϵ' at the entrance to the absorber.

The flux of alpha particles, ϕ_0 , is the number of alpha particles per cm^2 necessary to deliver one rad, as measured by an ionization chamber monitoring the incident beam at 230 MeV/u:

$$\phi_0 = (1.6 \times 10^{-8} \times (dE/dx)_{230})^{-1}. \quad (27)$$

The number of alphas incident at each source $I(\epsilon')$ in equation (22), per unit incident energy, is then given by:

$$I(\epsilon') = S_i \phi_0 / (\epsilon_2' - \epsilon_1'), \quad (28)$$

where S_i is the area presented by the source to the beam.

In order to calculate $N(E)$, a Fortran computer program, NEUTRA, was written for the Biomedical facility computer. The integrations in equation

(26) were performed numerically using Simpson's rule, and intervals $dZ_i = 1 \text{ g/cm}^2$ and $d\epsilon' = 10 \text{ MeV}$. The results were not sensitive to changes in the integration interval. The calculation for each detector position, using fifteen energy points E , takes about 20 sec on a PDP 11/45 computer, under the RSX11-M1 V3 operating system.

4.0 EXPERIMENTAL MEASUREMENTS AND TECHNIQUE

4.1 Beam Line Configurations

Exposures were made with the beam line configurations summarized in Table 2. Exposure B used the configuration most typical of that used in patient treatment, when a 15-cm diameter and 26-cm high water phantom was used to simulate the patient's head. The water column was filled with 16 cm of water so that the spread Bragg peak extended across the phantom. Configuration B' was similar to B except that the phantom was removed. In configuration A, the water degrader was emptied. Finally, configurations C through E successively removed one beam element in order to measure the effect of each upon secondary neutron production.

4.2 Neutron Detectors

The neutron intensity at several different locations was determined using activation detectors, moderated BF_3 counters, and thorium and bismuth fission counters. The characteristics of these detectors have been described in the literature (Cumming, 1963; Gilbert *et al.*, 1968). Some of their important characteristics are summarized in Table 3. The detectors in this table are divided into two groups--activation detectors and prompt counters. In the first group the radioactivity induced in the detector material was measured after irradiation in the LBL low-background facility (Wollenberg and Smith, 1966). Prompt counters were used with standard electronic counting apparatus. Beam intensities were kept at levels where no significant pile-up was observed.

4.3 Beam Monitors

4.3.1. Ionization chamber

The primary beam monitor used during these measurements was a standard Biomedical Division nitrogen-filled ionization chamber (ARC, 1977). This chamber was located immediately upstream of the spiral ridge filter. The beam was incident upon the chamber after passing through a brass collimator which limited the beam size at this point to a diameter of 14 cm. The energy of the beam monitored by the ionization chamber was ~230 MeV/u (920 MeV).

The presence of scattered particles may render the chamber sensitive to changes in the beam line attenuators described in section 2.0. A comparison with other beam monitors (cf. section 4.3.4) showed that the chamber was only sensitive to the presence of the spiral ridge filter (at the 3% level), an effect attributed to backscattered radiation to the extent that it is statistically significant.

All measurements were normalized to the dose indicated by this ionization chamber, in rad, using the conversion factor ϕ_0 calculated in section 3.0 to obtain the corresponding particle flux.

4.3.2. Aluminum monitor activation

An aluminum foil, which covered the upstream face of the brass collimator, was exposed to the alpha-particle beam during every irradiation. The ^{24}Na activity induced by the beam (Lindner and Osborne, 1953) was used to calculate the beam flux independently. Separate counting of the foil portion covering the collimator ring and the collimator opening showed that the fraction of the incident primary beam transmitted by the collimator

was 0.686 ± 0.004 . The reproducibility of this result served to provide assurance that the beam position was stable.

4.3.3. Auxiliary monitors

Two additional monitors were used, both of whose response was sensitive to beam line configurations. Moderated indium foils were used in both cases.

The first such monitor, "the patient table monitor," was located 60 cm from the beam line on the patient table (ISAH coordinates $x = +60$ cm; $y = 0$ cm; $z = 0$ cm), approximately at mid-torso for an irradiated patient.

The second auxiliary monitor was located near the doorway of the treatment area (at ISAH coordinates $x = -240$ cm; $y = -35$ cm; $z = +170$ cm) at a position judged to be minimally affected by changes in beam line configuration.

4.3.4. Intercomparison of monitor readings

Exposures were made with the beam line configurations given in Table 2 to study the influence of the beam elements on monitor reading. The experimental data obtained are given in Table 4. Errors in the data of this table are estimated as $\sim 1\%$ for the ionization chamber (short-term reproducibility), $\ll 1\%$ for the aluminum foil (counting statistics), and $\sim 1\%$ for the other monitors (counting statistics and reproducibility).

The patient table monitor is sensitive to beam line configuration (Table 4, column 5). The monitor reading increased by a factor of 1.6 when the spiral ridge filter was removed and by a factor of 2.0 when the lead collimator was additionally removed. These increased readings are simply due to an increase in the flux of helium ions falling on the Cerrobend collimator

(see Figure 10). When this element was removed, however, the monitor reading fell because the incident helium ions then had an unrestricted flight to the rear wall of the patient treatment room.

The response of the "doorway monitor" showed similar but smaller variations. When the spiral ridge filter was removed, the monitor reading increased. The subsequent removal of beam line elements produced a reversion to the original monitor reading--presumably because of a large number of mechanisms which happen to be roughly compensating in overall magnitude. Thus--somewhat fortuitously--the reading of the doorway monitor could be used as a check on the total number of helium ions entering the medical treatment area (within 40%).

4.4. Experimental Measurements

4.4.1. Major sources of neutrons

Measurements of neutron intensities in the biomedical cave, with the alpha beam at full intensity but with the steering magnet (which directs the beam into the biomedical cave) turned off and a beam plug in position, indicated no significant thermal or fast neutron flux density. The only significant production of neutrons in the biomedical cave is therefore due to primary beam particle interactions with objects along the beam in the cave itself.

Three main regions of beam interaction were found: (1) the wall collimator and spiral ridge filter; (2) the 12-cm lead collimator; and (3) the water column-Cerrobend collimator combination. These elements are shown in an enlarged view of the treatment room in Figure 10. The relative mag-

nitude of losses in these elements was studied in detail using aluminum activation detectors.

Neutron fluences were determined at a distance of 20 cm from the beam. A total of 29 aluminum disks were placed along the beam line at spacings varying between 5 cm and 20 cm (cf. Figures 5 and 6). Exposures were made with the several arrangements of the beam transport system summarized in Table 2. Known neutron sources were sequentially removed from the transport system.

The data obtained are shown in Figure 11. Curve A shows the neutron fluence profiles measured with the beam line configuration A, with no energy degrader or head phantom in position. A second exposure (curve B) was made to determine the neutron production in arrangement B, typically used in patient therapy. During this exposure the water phantom was placed in the beam at ISAH center to simulate the patient's head. The neutron fluence 20 cm from the beam and adjacent to the phantom was seen to increase during exposure B by a factor of 1.54 over that during exposure A. This increase is not surprising, since the water column is the main contributor to the neutron flux in the (X, Y, 0) plane and further downstream, and constitutes the main difference between configurations A and B. A similar result is indicated by the difference between curves B and C, which differ in the presence of the ridge filter and the water. A quantitative evaluation is not possible because the beam elements act as neutron shields as well as sources of neutrons.

The subsequent exposures C through E made it possible to identify the dominant neutron sources upstream of the Cerrobend collimator. Figure 12 shows the results of this analysis. The fluence profile measured for the normal beam line configuration (curve A) may be represented as the sum of

three source terms located at the spiral ridge filter, the edge of the iron pipe collimator downstream of the spiral filter, and the lead collimator (see Figure 10). These profiles are consistent with the hypothesis that each neutron source is dominated by an isotropic component, with a smaller component directed forward (see section 3.0). In patient treatment a fourth source of neutrons must be added--the energy degrader and the Cerrobend collimator.

Making the assumption that all these sources may be approximated by isotropic point sources, their strengths and locations may be estimated from the data of Figures 11 and 12. These source strengths may then be used to calculate the relative contributions to neutron fluence from the four major sources at locations along the patient table. Table 5 summarizes such calculations.

In interpreting these results, it is important to remember that the ^{27}Al - ^{24}Na measurements report the "14-MeV equivalent" flux densities (i.e., the flux density of monoenergetic 14-MeV neutrons that would produce the radioactivity observed in the sample). In the neutron spectra on the patient table, the number of neutrons above the 6-MeV threshold for the $^{27}\text{Al}(n,\alpha)^{24}\text{Na}$ reaction will be higher (by a factor of two to three) than the number of "14-MeV equivalent" neutrons.

Table 5 shows that out to distances of 50 cm from the beam axis, the water column and Cerrobend collimator combination is the dominant neutron source, but at greater distances the lead collimator is the largest source. These features are in agreement with calculations made using the methods described in section 3.0.

Further insight into the problem may be obtained from Figures 13 and 14.

Figure 13 shows the calculated (primary) neutron spectrum and the separate contributions of the main beam components at $X = 10$ cm. The same calculated relative contributions are plotted in Figure 14 for $X = 50$ cm. At low energies, where the neutron emission is assumed isotropic, the water column can be expected to yield more neutrons. The high-energy neutrons produced by the water column are detected at much greater angles than the high-energy neutrons produced by beam line elements further upstream. The angular dependence of the cross section for production of these neutrons results in the rapid decrease of the water column contribution above ~ 10 MeV, which is especially evident in Figure 14.

The result obtained with each activation detector depends on the threshold of the reaction used. For example, the $^{27}\text{Al} + ^{18}\text{F}$ reaction, with a threshold of ~ 40 MeV, will show a smaller relative contribution of the water column to the neutron flux than the moderated BF_3 counter which has a threshold of ~ 1 eV. The results of Figures 11 and 12 are in agreement with the calculated relative contributions, taking into account the threshold of the $^{27}\text{Al} + ^{24}\text{Na}$ reaction.

4.4.2 Variation of neutron fluence along the patient table

Estimates of the absorbed doses to patients may be obtained from measurements of the neutron spectrum. Such spectra can be obtained, at least approximately, by measurement of neutron fluences with detectors of different energy response. These measurements were made using configurations B and B' (Table 2), with and without the phantom described earlier.

Data without the phantom. Measurements of neutron fluence with no head phantom in place were made using a moderated BF_3 counter, the aluminum

and carbon activation reactions, and a bismuth fission counter. The water column was filled to 16 cm.

Measurements with the moderated BF_3 counter extended out to 2.1 m from the beam axis. Measurements with the activation detectors were made for $X = 10$ to 78 cm from the beam axis, and measurements with the bismuth fission counter extended out to 50 cm. The results of these measurements are shown in Figure 15.

Data could not be taken at distances closer than 10 cm from the beam axis without exposing the detectors to the primary beam. Estimates of neutron fluence on the beam axis therefore depend upon an extrapolation of the data shown in Figure 15. This extrapolation was made using the assumption that the high-energy neutron yields had a gaussian profile centered on the beam axis, with a tail given by the rising portion of the measured curves shown in this figure. The moderated BF_3 data were extrapolated linearly. The poor statistics obtained with the bismuth fission counter did not provide enough points for an extrapolation to $X = 0$, and the assumption was made that the extrapolated portion had the same shape as the ^{18}F results (which correspond to the next highest threshold). The extrapolated portions of the data are also shown in Figure 15.

Assuming that the extrapolated value of the BF_3 counter corresponds to an integral of the neutron spectrum at 0° , the value obtained is $\sim 1.2 \times 10^5 \text{ n/cm}^2$ per rad of incident alpha particles (corresponding to about 0.3 neutrons/alpha). This is significantly less than that shown for the $^{12}\text{C} \rightarrow ^{11}\text{C}$ and $^{27}\text{Al} \rightarrow ^{18}\text{F}$ activation detectors. This is due to the neutron energy response of the detectors and to activation by secondary protons. This problem is discussed in the next section.

Head phantom data. Similar measurements were made with the head phantom in place, and with the water column filled to 16 cm to stop the alpha-particle beam within the phantom. The results of these measurements are shown in Figure 16. The data were extrapolated according to the same method used for the no-phantom data. A slightly increased secondary particle flux was measured by the proton-sensitive activation detectors, but the width of the distribution did not change significantly.

These detector data were used to unfold the particle spectra on the assumption that they consisted entirely of neutrons. This assumption is not strictly true. However, it is a useful departure point for an iterative calculation of the neutron spectrum, as discussed in section 4.5.

4.5 Secondary-Particle Spectra and Absorbed Dose Calculations

Spectra were calculated at locations on the patient table for $X = 0$ to 50 cm, using the unfolding routine LOUHI computer program (Routti, 1969). The spectra on the beam axis and at 5 cm are based on data extrapolated as described in section 4.4.2.

The shapes of the spectra are not well determined below ~0.1 MeV because only one detector--the moderated BF_3 counter--responded to neutrons below 6 MeV. However, only a small fraction of the absorbed dose is deposited by low-energy neutrons and the precise shape of the spectrum below 0.1 MeV is therefore not important.

The following considerations show how an estimate of the neutron spectrum alone may be obtained using the spectra unfolded by LOUHI. Given a flux density of $\phi_j(E)$ particles of type j (per $\text{cm}^2 \text{ MeV rad}$), let the reaction i

be produced in an activation detector with a cross section $\sigma_{ij}(E)$. Then, the observed counting rate in the detector, C_i , due to particles j , will be:

$$C_{ij} = K_i \int_0^{\infty} \sigma_{ij}(E) \phi_j(E) dE , \quad (29)$$

where K_i combines geometry and counting efficiency factors. If the particles are restricted to neutrons and protons ($j = n, p$), the total counting rate will be:

$$C_i = K_i \int_0^{\infty} (\sigma_{in}(E) \phi_n(E) + \sigma_{ip}(E) \phi_p(E)) dE . \quad (30)$$

Let

$$R(E) = \phi_p(E)/\phi_n(E) \quad \text{and} \quad r_i(E) = \sigma_{ip}(E)/\sigma_{in}(E) .$$

Then

$$C_i = K_i \int_0^{\infty} (1 + R(E)r_i(E)) \sigma_{in}(E) \phi_n(E) dE . \quad (31)$$

Given a set of observed C_i , let us call $\phi'_n(E)$ the flux density obtained by unfolding equation (31) under the assumption that $Rr_i = 0$ (i.e., that all the flux is due to neutrons). Then, since the C_i are fitted by the procedure, by definition

$$C_i = K_i \int_0^{\infty} \sigma_{in}(E) \phi'_n(E) dE . \quad (32)$$

For this to be true, it is sufficient that:

$$\phi'_n(E) = \{1 + R(E)r_i(E)\} \phi_n(E) . \quad (33)$$

Therefore, the "true" neutron fluence will be

$$\phi_n(E) = \phi'_n(E)/\{1 + R(E)r_i(E)\} \quad (34)$$

and, with the assumption $R(E) = 1$ (implicit in the calculation described in section 3.0), we obtain

$$\phi_n(E) = \phi'_n(E)/\{1 + r_i(E)\} . \quad (35)$$

Equation (33) is, of course, not a necessary condition, since equations (30) and (33) can still be satisfied if the integration over the region where $R(E)$ and $r_i(E)$ are different from zero averages to the correct counting rate. Furthermore, $R(E)$ cannot be defined independently if the counting rate constraints are to be valid. However, equation (35) can be thought of as an approximation to the "best" unfolded spectrum. A self-consistent calculation would then require that the separated neutron and proton spectra be introduced into the calculation for further iteration.

The result of these calculations is shown in Figure 17 for $X = 10$ cm. The broken curve shows the spectrum unfolded under the assumption that all the particles are neutrons. The full curve shows the neutron spectrum obtained using equation (35) and the $r_i(E)$ ratios for the production of ^{11}C . The region below about 20 MeV, where both the $(n, 2n)$ and the (p, pn) cross sections

go to zero, has been smoothly joined to the low-energy part of the curve by hand. As noted above, the use of equation (35) with the ratios for another detector would have resulted in a somewhat different corrected neutron spectrum. However, further iterations will not yield substantial modifications of the shape of the curve. In addition, our interest in integral properties of the neutron fluence, which are largely insensitive to spectral shape, makes this approximation adequate.

The assumption that $R(E) = 1$ is not necessarily realistic, and can be seen to be inconsistent with the results shown in Figure 17. On the other hand, the results of Figure 17 are consistent with the qualitative features to be expected for the proton spectrum, mainly an energy cutoff at both the high and low ends. The high-energy cutoff results from the fact that most protons will have to traverse portions of the various particle sources along the beam line, with the consequent ionization losses. At low energies, a loss in counting rates is to be expected for protons with residual ranges less than the activation detector thickness. The low- and intermediate-energy proton flux will, of course, be augmented by the energy degradation of protons at higher energies.

The open circles in Figure 17 are the results of the calculation described in section 3.0. It is evident that the theoretical calculation overestimates the fraction due to evaporation neutrons ($E = 0.1$ to 10 MeV) as well as that due to high-energy neutrons ($E \geq 150$ MeV) and underestimates the intermediate-energy neutrons ($E = 20$ to 100 MeV).

This trend of the comparison is to be expected, since the calculation assumes that no other secondaries are produced, and only removal results from further interaction of secondaries in the beam elements. However,

one must expect the neutrons calculated to have energies above approximately 100 MeV to cascade in the beam material and reappear at lower energies, filling up the intermediate energy region. Similarly, one would expect some of these intermediate energy neutrons, as well as the evaporation neutrons, to suffer multiple interactions and become depleted. The resulting experimental neutron spectrum would thus have the well-known slow and thermal neutron tail (not measured in this work). Thus, a qualitative change of the calculated (primary) neutron spectrum to yield the shape of the unfolded (multiple scattered) neutron spectrum is to be expected.

In order to evaluate the degree of quantitative agreement between the two spectra, it must be remembered that both spectra suffer from intrinsic uncertainties. The calculated theoretical spectrum properly refers to primary neutrons. The unfolded spectrum is obtained by optimizing a solution to an underdetermined problem, i.e., the number of detectors is much less than the number of energy bins. The unfolding procedure, constrained to yield only "reasonable" spectra that reproduce the detector counting rate, does not provide a single, unambiguous solution. This is a drawback if differential spectra are needed. On the other hand, it makes the determination of integrated quantities, such as dose, insensitive to the exact shape of the spectrum within rather broad limits.

The integral quantity of greatest interest is, of course, the absorbed dose. Table 6 summarizes the experimental results, the values of detector response computed by LOUHI, and the calculated absorbed dose obtained by attributing the spectrum entirely to neutrons, at the various detector positions along X. These values are expressed in terms of absorbed dose per rad deposited by the primary beam in the plateau region (cf. section 4.3.1).

Under normal conditions the tumor volume is irradiated with a stopping beam (the extended Bragg region); the absorbed dose delivered by the alpha particles will be higher by a factor of about 1.4 (thus reducing the relative contribution of the neutrons by a similar amount).

In order to compare the values of absorbed dose given in Table 6 with the results that can be obtained from the theoretical spectra, the fluence-to-dose conversion factors must be known. Rindi has derived these from the work of many authors, and estimates their errors to be approximately 25% (1977). The values of these conversion factors have been tabulated in Table 7, and were used in deriving the absorbed dose estimates given in Table 6. The similar quantities for protons have been calculated and compared with experiment by Armstrong and Bishop (1971). The absorbed dose due to protons increases as a function of depth. At the maximum dose, the corresponding conversion factor of protons will be three to five times greater than that for neutrons. This ratio was used as a conservative estimate of the proton dose.

The absorbed dose calculated using the theoretical spectra at $X = 10$ cm (Figure 17) was found to be 0.4% of the primary alpha-particle dose. These values can be compared with the result of Table 6, i.e., 0.25%. This agreement is encouraging. In view of the preceding discussion, the absorbed dose values quoted in Table 6 can be taken as a conservative estimate of incidental dose to a patient in a "worst case" beam configuration.

5.0 SUMMARY AND CONCLUSIONS

The major sources of secondary particles along the alpha-particle beam of the Lawrence Berkeley Laboratory 184-inch synchrocyclotron have been identified. They are: the water column/Cerrobend collimator combination, the lead collimator, the upstream edge of the iron pipe collimator #1, and the spiral ridge filter. In the approximation of a point source, these have relative source strengths in the proportion 1:5:1:4, respectively. The contribution of the water column predominates in the forward direction, while the lead collimator contributes mainly at large angles. Thus, neutrons and protons produced in the water column account for more than 75% of the secondary-particle absorbed dose to the patient.

The activation detectors cannot distinguish charged particles, mainly protons, from neutrons. However, the calculated spectra provide a conservative estimate for the dose absorbed by the patients during therapy. The absorbed dose, calculated from these spectra, is dominated by the total particle flux above 0.1 MeV; it is not sensitive to variations in the energy spectrum. Therefore, it may be concluded that the reported estimates of dose due to "neutrons" can be confidently taken as an upper-limit estimate.

There was no significant contribution to the radiation field from sources external to the patient treatment room.

The absorbed dose to the patient due to secondary particles may be reduced in several ways: (1) locating regions of primary beam interactions as far as possible from the patient; (2) limiting the interaction of the primary helium beam with beam line elements; (3) utilizing the minimum thickness of scattering material in the primary beam; or (4) optimizing stopping power vs nuclear interaction length in the beam elements.

The degree of primary beam interaction is to some extent determined by the size of the field required to irradiate the patient. The measurements described in this paper were made with a lead scatterer designed to produce a field 30 cm in diameter. However, more typical radiation fields used in patient treatment are 20 cm in diameter. A thinner (0.45 cm) lead scatterer is required to produce the smaller field, resulting in fewer neutrons produced in the scatterer and in less primary beam interaction with beam transport elements.

In the present facility, most of the neutron sources are located as far as possible from the patient. The scattering foil and spiral ridge filter are located close to the main cyclotron vault shielding. The iron pipes and lead collimator are placed as far upstream as possible while yielding an acceptable image at the Cerrobend collimator. The size of the lead collimator is determined by the field size required, which in turn determines the size of the Cerrobend collimator. Lead collimators with apertures of 12-cm, 14.5-cm, 17-cm, and 25-cm diameter are used.

The Cerrobend collimator must be as close as possible to the patient in order to maintain a sharp definition of the radiation field.

The major source of secondary neutrons at the patient position is the water column used as an energy degrader. In principle, it may be possible to locate this beam line element upstream of the ridge filter, at a loss of accessibility. In such a configuration, the water column could be a part of the multiple scattering target used for beam flattening. This has a disadvantage in that different lead foil thicknesses are required to compensate for different water column thicknesses, but it has the advantage of significantly reducing in neutron dose.

With one exception, changes in the material used to make the energy degrader will have only a small effect. This is due to the fact that, for equal stopping power, the required thickness in g/cm^2 will be relatively constant. The number of interactions, $n \times \sigma$, will be proportional to $A^{-1/3}$, and they will depend on n (proportional to $1/A_t$) and σ (proportional to $A_t^{2/3}$). Thus, as A increases the number of nuclei per cm^3 for equal stopping power decreases. A calculation shows that, to a first approximation, a uranium degrader would produce about 78% of the nuclear interactions expected for water.

The exception noted above is a hydrogen energy degrader, which has no target neutrons and twice the stopping power of water (due to its Z/A ratio of one). Thus, in principle, a liquid hydrogen absorber may be an optimum, but impractical, choice for the energy degrader.

The measurements give an upper limit of the absorbed dose in soft tissue due to neutrons and protons that decreases from about 3×10^{-3} rad on the beam axis to about 1×10^{-3} rad at 20 cm from the beam axis, per rad of incident beam. Thus, provided the eye is outside the alpha-particle radiation field, the absorbed dose to the lens of the eye due to secondary particle contamination (considered to consist entirely of neutrons) will typically be about 10 rad or less, which is well below the threshold for the incidence of cataracts reported for photons and fission neutrons.

The dose to the red bone marrow will be lower by about an order of magnitude. If we take an upper limit of the risk of leukemia incidence to be $4 \times 10^{-4} \text{ rad}^{-1}$, an upper limit to the risk of leukemia following irradiation of the head by the helium-ion beam is 0.04%.

These results suggest that major modifications to the present beam line are not warranted by the risk due to the absorbed dose deposited by secondary neutrons and protons outside the treatment volume.

Acknowledgement

This study has been supported by NIH Grant 5P01CA19138, and the Biomedical and Environmental Research Division of the Department of Energy.

REFERENCES

- ARC (Accelerator Research Coordination). 1977. Bevatron/Bevalac User's Handbook, Biology and Medicine. Available from Accelerator Research Coordination Office (ARC), Lawrence Berkeley Laboratory, University of California, Berkeley.
- Armstrong, T. W. and Bishop, B. L. 1971. Calculation of the absorbed dose and dose equivalent induced by medium-energy neutrons and protons and comparison with experiment. Radiation Research 47, 581-588.
- Bailey, L. 1956. Angle and energy distribution of charged particles from the high-energy nuclear bombardment of various elements. Lawrence Berkeley Laboratory Report UCRL-3334 (Ph.D. thesis, University of California, Berkeley).
- Bertini, H. W. 1963. Low-energy intranuclear cascade calculation. Phys. Rev. 131, 1801-1821.
- Bowman, W. W. and Blann, M. 1969. Nuclear Physics A131, 513-531.
- Castro, J. R., Quivey, J. M., Lyman, J. T., Chen, G. T. Y., Tobias, C. A., Kanstein, L. L., and Walton, R. E. 1977. Heavy-ion therapy. In Biological and Medical Research with Accelerated Heavy Ions at the Bevalac, 1974-1977. Lawrence Berkeley Laboratory Report LBL-5610, pp. 198-218, University of California, Berkeley.
- Chamberlain, O. 1960. Optics of high-energy beams. Annual Rev. Nuclear Sci. 10, 161-192.
- Church, L. B. 1972. Study of (α , αn) reactions with 900-MeV ions. Phys. Rev. C 6, 1293-1297.
- Crowe, K., Kanstein, L., Lyman, J., and Yeater, F. August 1975. A large-field medical beam at the 184-inch synchrocyclotron. Lawrence Berkeley Laboratory Report LBL-4235, University of California, Berkeley.

- Cumming, J. B. 1963. Monitor reactions for high-energy proton beams. Ann. Rev. Nuclear Sci. 13, 261-286.
- Deutsch, R. W. 1955. Analysis of secondary particles resulting from high-energy nuclear bombardment. Phys. Rev. 97, 110-1123.
- Gabriel, T. A., Santoro, R. T., and Alsmiller, R. B. 1970. An approximate high-energy alpha-particle nucleus-collision model. Oak Ridge National Laboratory Report ORNL-TM-3153, Oak Ridge, Tennessee.
- Ghiorso, A., Grunder, H., Hartsough, W., Lambertson, G., Lofgren, E., Lou, K., Main, R., Mobley, R., Morgado, R., Salsig, W., and Selph, F. 1973. The Bevalac--An economical facility for very energetic heavy-particle research. IEEE Trans. Nuclear Sci. NS-20, 155-158.
- Gilbert, W. S. et al. September 1968. 1966 CERN-LRL-RHEL shielding experiment at the CERN proton synchrotron. Lawrence Berkeley Laboratory Report UCRL-17941, University of California, Berkeley.
- Goebel, K. and Miller, A. J. 1971. Intensity estimation for a neutron beam for biological and medical applications. Nuclear Instr. Meth 96, 581-587.
- Grunder, H. A., ed. 1974. Heavy-ion facilities at the Lawrence Berkeley Laboratory. Lawrence Berkeley Laboratory Report LBL-2090, University of California, Berkeley.
- Grunder, H. A. and Selph, F. B. 1977. Heavy-ion accelerators. Ann. Rev. Nuclear Sci. 27, 353-392.
- Gutbrod, H. H., Sandoval, A., Johanssen, P. J., Poskanzer, A. M., Gosset, J., Meyer, W. E., Westfall, G. D., and Stock, R. 1976. Final state interactions in the production of hydrogen and helium isotopes by relativistic heavy ions on uranium. Phys. Rev. Lett. 37, 667-670.

- Ham, W. T. 1960. Fast neutron radiation hazards. In Fast Neutron Physics, edited by J. Marion and J. L. Fowler. New York: Interscience, p. 841.
- Hodgman, C. D., ed. 1959. Handbook of Chemistry and Physics, 41st ed. Cleveland: Chemical Rubber Publishing Co.
- Kanstein, L. L., Smith, A. R., and Thomas, R. H. 5 September 1975. The absorbed dose due to neutron contamination around the periphery of the alpha-particle beam of the 184-inch synchrocyclotron. Health Physics Department Internal Note, HPN-37.
- Karol, P. J. 1975. Nucleus-nucleus reaction cross sections at high energies: soft sphere model. Phys. Rev. C 11, 1203-1209.
- Lawrence, J. and Tobias, C. A. February 1965a. Annals of Internal Medicine 62, 2.
- Lawrence, J. and Tobias, C. A. 1965b. Progress in Atomic Medicine, pp. 127-146.
- Lindner, N. and Osborne, R. 1953. The cross section for the reaction $\text{Al}^{27}(\alpha, \alpha_2\text{pn}) \text{Na}^{24}$ from threshold to 380 MeV. Phys. Rev. 91, 342.
- Radin, J. 1970. Cross section for $\text{C}^{12}(\alpha, \alpha_n) \text{C}^{11}$ at 920 MeV. Phys. Rev. C 2, 793-798.
- Radin, J. R., Smith, A. R., and Little, N. 1974. Alpha-spallation cross sections at 920 MeV (230 MeV/u) in ^{27}Al , ^{16}O , ^{12}C , and ^9Be , and applications to cosmic-ray transport. Phys. Rev. C 9, 1718.
- Rindi, A. 1977. An analytical expression for the neutron flux-to-absorbed dose conversion factor. Health Physics 33, 264.
- Rossi, H. H. and Kellerer, A. M. 1974. The validity of risk estimates of leukemia incidence based on Japanese data. Radiation Research 58, 131-140.
- Routti, J. T. April 1969. High-energy neutron spectroscopy with activation detectors, incorporating new methods for the solution of Fredholm equations.

- Lawrence Berkeley Laboratory Report UCRL-18514. (Ph.D. thesis, University of California, Berkeley).
- Saito, T. 1975. The nucleus-nucleus inelastic cross sections at cosmic-ray energies. J. Phys. Soc. Japan 38, 282.
- Schimmerling, W., Devlin, T. J., Johnson, W. W., Vosburgh, K. G., and Mischke, R. E. 1973a. Neutron-nucleus total and inelastic cross sections: 900 to 2600 MeV/c. Phys. Rev. C 7, 248-262.
- Schimmerling, W., Vosburgh, K. G., and Todd, P. W. 1973b. Measurements of range in matter for relativistic heavy ions. Phys. Rev. B 7, 2895-2899.
- Schneider, R., Schmidt, R. A., and Kühler, A. M. 1974. Preparations for cancer therapy at the Harvard cyclotron. Bull. Amer. Phys. Soc. 19, 31.
- Serber, R. 1947. The production of high-energy neutrons by stripping. Phys. Rev. 72, 1008-1016.
- Smith, A. R. 25 August 1975. Dose rate due to neutrons around the alpha-particle beam of the 184-inch synchrocyclotron. Health Physics Department Internal Note HPN-35.
- Tobias, C. A. 1973. Pretherapeutic investigations with accelerated heavy ions. Radiology 108, 145-158.
- Upton, A. C. 1968. Effects of radiation on man. Annual Review of Nuclear Science 18, 495.
- Westfall, G. D., Gossett, J., Johansen, P. J., Poskanzer, A. M., Meyer, W. G., Gutbrod, H. H., Sandoval, A., and Stock, R. 1976. Nuclear fireball model for proton inclusive spectra from relativistic heavy-ion collisions. Phys. Rev. Lett. 37, 1202-1205.
- Wollenberg, H. A. and Smith, A. R. 1966. A concrete low-background counting enclosure. Health Physics 12, 53-60.

Table 1. Location of Beam Shaping Devices

Z (m)	Element
0	Patient position (ISAH center)
- 0.21	Cerrobend collimator
- 0.285	
- 0.75	
- 1.57	Lead collimator
- 1.66	
- 3.00	
- 3.05	Iron pipe #1
- 3.83	
- 4.23	Iron pipe #2
- 4.50	
- 4.83	Spiral ridge filter
	Ionization chamber
	Brass collimator

Table 2. Beam Line Configurations

Exposure (See Fig. 11)	Brass Collimator	Spiral Ridge Filter	Lead Collimator	Water Column (cm, water)	Cerrobend Collimator	Head Phantom
A	In	In	In	0.0	In	Out
B	In	In	In	16.0	In	In
B'	In	In	In	16.0	In	Out
C	In	Out	Out	0.0	In	Out
D	In	Out	Out	0.0	In	Out
E	In	Out	Out	0.0	Out	Out

Table 3. Summary of Neutron Detector Properties

Detector Material	Reaction	Detector Size	Approximate Energy Range	Response** cpm/n cm ⁻² s ⁻¹	Background Rate c/min
A. ACTIVATION DETECTORS					
1. Indium (moderated by 6" paraffin)	$^{115}\text{In}(n,\gamma)^{116}\text{In}$	1" diam X 0.005" (~ 0.5 grams)	1 eV + 20 MeV	10 c/min (gfp)	10.0 (gfp)***
2. Aluminum	$^{27}\text{Al}(n,\alpha)^{24}\text{Na}^*$	2" diam X 1/8" 2" X 2" X 1/8" 4" diam X 1"	>6 MeV >6 MeV >6 MeV	0.85 1.12 21.2	69.0 (NaI) 69.0 (NaI) 70.0 (NaI)
3. Polystyrene Polyethylene	$^{12}\text{C}(n,2n)^{11}\text{C}^*$	2" X 2" X 3/4" 4" diam X 1/2"	>20 MeV >20 MeV	1.4 2.7	44.0 (NaI) 44.0 (NaI)
4. Aluminum	$^{27}\text{Al} + ^{18}\text{F}^*$	2" X 2" X 1/8"	>40 MeV	0.11	44.0 (NaI)
B. PROMPT COUNTERS					
5. BF ₃ Counter (moderated by 3" paraffin)	$^{10}\text{B}(n,\alpha)^7\text{Li}$	8" length X 1" diam	1 eV + 20 MeV	1.0	-
6. Parallel plate ion chamber	$^{232}\text{Th}(n,f)^*$	5-cm diam plates	>2 MeV	~ 0.02	-
7. Parallel plate ion chamber	$^{209}\text{Bi}(n,f)^*$	5-cm diam plates	>50 MeV	0.02	-

* These reactions can also be induced by protons which have energies sufficiently high to penetrate the Coulomb barrier of target nuclei.

** These values were obtained from calibrations in which detectors were irradiated with neutrons of known energy and intensity.

*** (gfp) refers to a gas-flow proportional counter operated to detect β -particles.

Table 4. Intercomparison of Monitor Data (arbitrary units)

Exposure (Fig.10)	Experimental Details	Ionization Chamber*	Al foil Monitor**	Patient Table Monitor***	Doorway Monitor***
A	All beam elements in place	3352 (1.03)	6.02×10^5 (1.00)	1.73×10^5 (1.00)	5.66×10^4 (1.00)
C	Spiral ridge filter removed	3257 (1.00)	6.07×10^5 (1.00)	2.74×10^5 (1.58)	7.69×10^4 (1.36)
D	Spiral ridge filter and lead colli- mators removed	3222 (0.99)	5.93×10^5 (0.99)	3.43×10^5 (1.98)	5.43×10^4 (0.96)
E	Spiral ridge filter, lead and Cerro- bend colli- mator removed	3255 (1.00)	6.00×10^5 (1.00)	1.14×10^5 (0.66)	5.57×10^4 (0.98)

* Figures in parentheses are the ratio of the measured value to the average value of exposures C, D, and E.

** Figures in parentheses are the ratio of the measured value to the average value.

*** Figures in parentheses are the ratio of the measured value to the value measured in exposure A.

Table 5a. Point Source Strengths

Z Location Along Beam Line (cm)	Beam Element	Source Strength per Incident Rad (n/sec)
- 25	Water column/Cerrobend collimator	1.5×10^8
-165	Lead collimator	7.0×10^8
-350	Iron pipe	1.7×10^8
-420	Spiral ridge filter	6.0×10^8

Table 5b. Relative Fluence Contribution

X Location on Patient Table (cm)	Fluence Contribution From:			
	Water Column and Cerrobend Collimator	Lead Collimator	Iron Pipe	Spiral Ridge Filter
0	89%	9.2%	0.5%	1.2%
50	64%	30%	1.7%	4.3%
100	39%	49%	3.4%	8.6%
150	27%	56%	4.6%	12%
200	21%	57%	5.7%	15%

Table 6a. Summary of Results Obtained with Computer Program LOUHI: No Phantom at Treatment Position

Position	Reaction/ Detector	Measured Response (n cm ⁻² primary beam rad)	Calculated Response (n cm ⁻² primary beam rad)	Absorbed Dose (rad/primary beam rad)*
0 cm	$^{27}\text{Al} \rightarrow ^{24}\text{Na}$	6.0×10^4	6.0×10^4	3.33×10^{-3}
	Moderated BF ₃ counter	1.10×10^5	1.10×10^5	
	$^{12}\text{C} \rightarrow ^{11}\text{C}$	2.90×10^5	2.88×10^5	
	$^{27}\text{Al} \rightarrow ^{18}\text{F}$	1.65×10^5	1.66×10^5	
5 cm		5.5×10^4	5.5×10^4	2.97×10^{-3}
		1.08×10^5	1.08×10^5	
		2.50×10^5	2.47×10^5	
		1.45×10^5	1.46×10^5	
10 cm		4.4×10^4	4.4×10^4	2.49×10^{-3}
		1.05×10^5	1.05×10^5	
		2.06×10^5	2.03×10^5	
		1.16×10^5	1.17×10^5	
15 cm	$^{27}\text{Al} \rightarrow ^{24}\text{Na}$	2.50×10^4	2.51×10^4	1.35×10^{-3}
	Moderated BF ₃ counter	1.01×10^5	1.01×10^5	
	$^{12}\text{C} \rightarrow ^{11}\text{C}$	8.5×10^4	8.5×10^4	
	BiF	1.46×10^4	1.46×10^4	
	$^{27}\text{Al} \rightarrow ^{18}\text{F}$	4.40×10^4	4.43×10^4	
20 cm		1.84×10^4	1.85×10^4	1.10×10^{-3}
		9.8×10^4	9.8×10^4	
		6.8×10^4	6.8×10^4	
		2.89×10^4	2.90×10^4	

*The primary beam rad used here is that in the plateau region. The dose to the irradiated tumor is a factor of about 1.4 higher.

Table 6a. (cont'd.)

Position	Reaction/ Detector	Measured Response (n cm ⁻² primary beam rad)	Calculated Response (n cm ⁻² primary beam rad)	Absorbed Dose (rad/primary beam rad)*
30 cm	$^{27}\text{Al} \rightarrow ^{24}\text{Na}$	1.78×10^4	1.79×10^4	1.15×10^{-3}
	Moderated BF ₃ counter	9.4×10^4	9.4×10^4	
	$^{12}\text{C} \rightarrow ^{11}\text{C}$	6.8×10^4	6.8×10^4	
	BiF	1.21×10^4	1.20×10^4	
	$^{27}\text{Al} \rightarrow ^{18}\text{F}$	3.57×10^4	3.58×10^4	
50 cm		1.54×10^4	1.55×10^4	1.21×10^{-3}
		8.6×10^4	8.6×10^4	
		6.3×10^4	6.2×10^4	
		2.22×10^4	2.21×10^4	
		3.32×10^4	3.38×10^4	

Table 6b. Summary of Results Obtained with Computer Program LOUHI: Phantom at Treatment Position

0 cm	$^{27}\text{Al} \rightarrow ^{24}\text{Na}$	8.00×10^4	8.06×10^4	4.64×10^{-3}
	Moderated BF_3 counter	1.50×10^5	1.50×10^5	
	$^{12}\text{C} \rightarrow ^{11}\text{C}$	4.15×10^5	4.08×10^5	
	$^{27}\text{Al} \rightarrow ^{18}\text{F}$	2.35×10^5	2.37×10^5	
5 cm		7.10×10^4	7.15×10^4	3.96×10^{-3}
		1.30×10^5	1.30×10^5	
		3.50×10^5	3.45×10^5	
		2.00×10^5	2.01×10^5	
10 cm		5.40×10^4	5.42×10^4	2.83×10^{-3}
		1.05×10^5	1.05×10^5	
		2.40×10^5	2.38×10^5	
		1.43×10^5	1.44×10^5	
15 cm	$^{27}\text{Al} \rightarrow ^{24}\text{Na}$	2.70×10^4	2.71×10^4	1.27×10^{-3}
	Moderated BF_3 counter	1.01×10^5	1.01×10^5	
	$^{12}\text{C} \rightarrow ^{11}\text{C}$	9.50×10^4	9.42×10^4	
	BiF	1.70×10^4	1.70×10^4	
	$^{27}\text{Al} \rightarrow ^{18}\text{F}$	5.10×10^4	5.13×10^4	

FIGURE LEGENDS

- Figure 1: Plan view of the 184-inch synchrocyclotron.
- Figure 2: Plan view of the biomedical cave of the 184-inch synchrocyclotron.
- Figure 3: Schematic diagram of the beam transport system of the biomedical cave showing collimators and scatterers.
- Figure 4: Schematic diagram of the patient treatment area. The ISAH coordinate system is shown (see text).
- Figure 5: General view of the beam line in the biomedical cave. The spiral ridge filter is to the left; the two iron collimating pipes and lead collimator are in the center.
- Figure 6: Close-up view showing Cerrobend collimator, water column, and lead collimator (radiation detectors may be seen in position in the photograph).
- Figure 7: Double differential cross sections replotted from Westfall et al. (1976), for 400 MeV/u alpha particles incident on uranium. The lines passing through the low-energy points have been drawn by eye for use in the present work.
- Figure 8: The "evaporation" and "central collision" cross sections calculated as described in the text for comparison with the data of Bailey

(1956) for 205 MeV/u alpha particles incident on aluminum. The full curve represents the trend of Bailey's results (errors typically are 10%). The open circles are calculated points using equation (2), and the open squares are calculated using equations (21) and (22), with a gaussian cutoff at energies below 12.5 MeV at an average angle of 4.8° . The broken curve is obtained integrating the data of Gutbrod et al. (1976) directly, and dividing by the solid angle (0° to 65°) corresponding to Bailey's measurements.

Figure 9: The three types of cross sections calculated as described in the text, at an angle of $\sim 13^{\circ}$ (corresponding to a detector position on the x-axis of 10 cm), for 185 MeV/u alpha particles incident on water.

Figure 10: Plan view showing location of beam line elements.

Figure 11: Neutron fluence profiles along the beam line, measured by the $^{27}\text{Al} \rightarrow ^{24}\text{Na}$ reaction, for the beam line configurations given in Table 2. The equivalent 14-MeV flux density is shown.

Figure 12: Analysis of neutron fluence profiles. The heavy solid curve shows the experimentally determined profile, and the dashed curves show the profiles for the three major sources of neutrons.

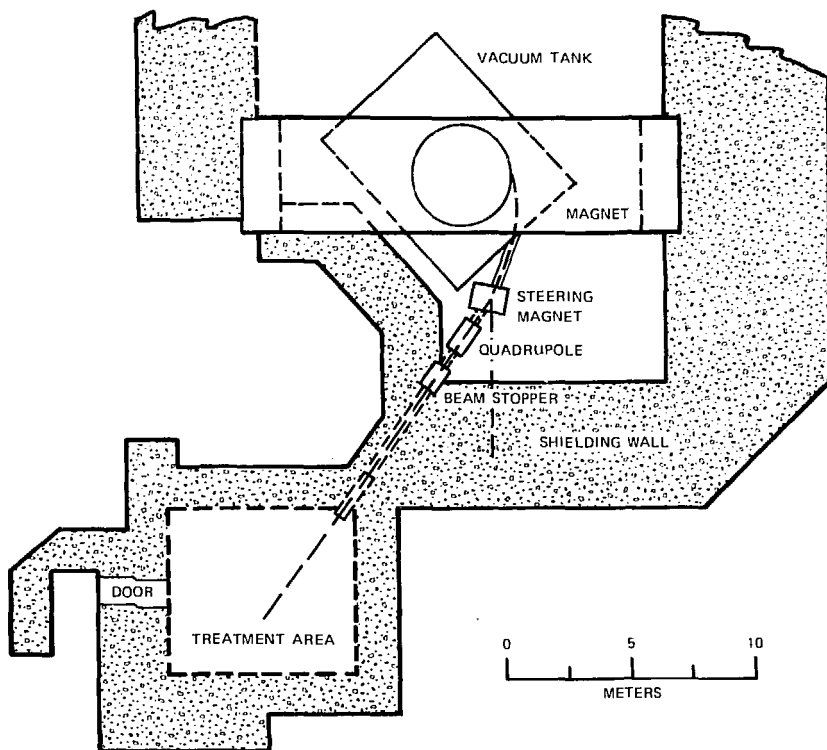
Figure 13: Contribution of the various components to the calculated neutron flux at 10 cm from the beam axis.

Figure 14: Contribution of the various components to the calculated neutron flux at 50 cm from the beam axis.

Figure 15: Neutron fluence, as a function of distance from ISAH center, measured along the patient table with five detectors. (No head phantom in place; 16-cm water energy degrader.) The equivalent 14-MeV flux density is given for the $^{27}\text{Al} + ^{24}\text{Na}$ reaction.

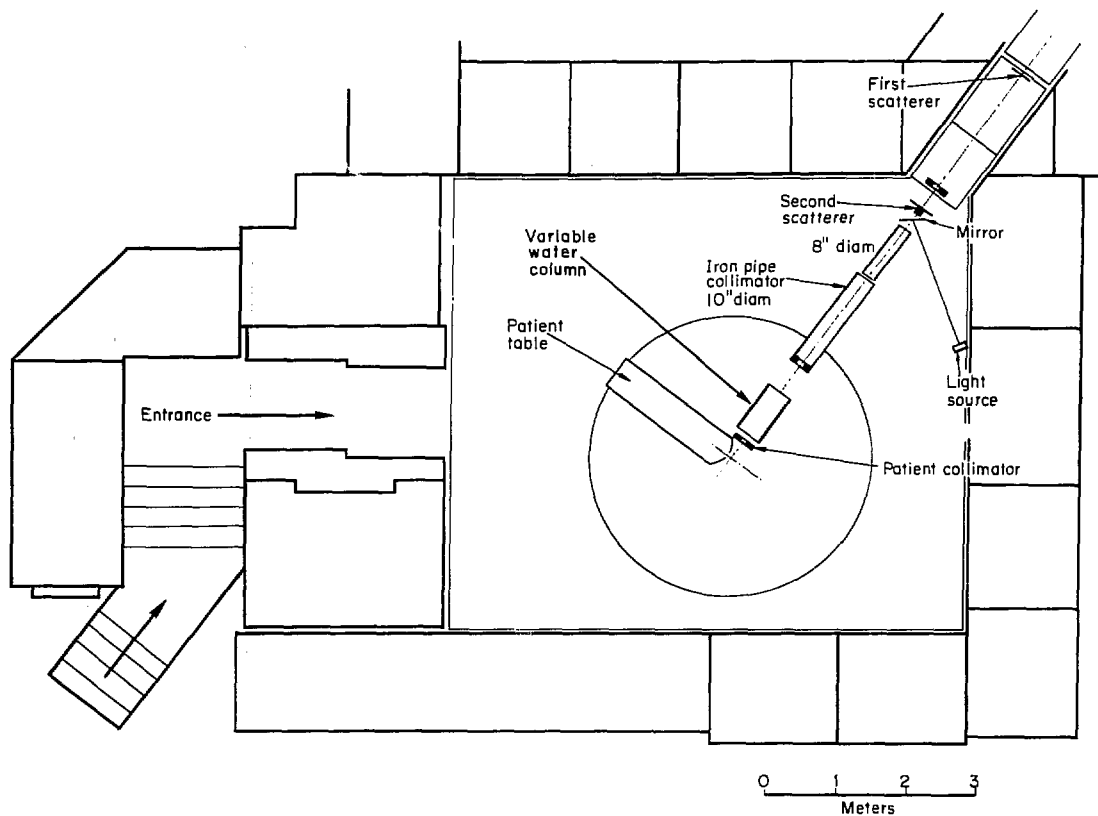
Figure 16: Neutron fluence, as a function of distance from ISAH center, measured along the patient table with four detectors. Head phantom in place; 16-cm water energy degrader. The equivalent 14-MeV flux density is given for the $^{27}\text{Al} + ^{24}\text{Na}$ reaction.

Figure 17: Unfolded spectrum obtained from the detector measurements, assuming entire spectrum due to neutrons (broken curve), unfolded spectrum corrected to estimate neutron spectrum only (cf. text) (full curve), and calculated neutron spectrum using the model developed in section 3.0 (open circles).



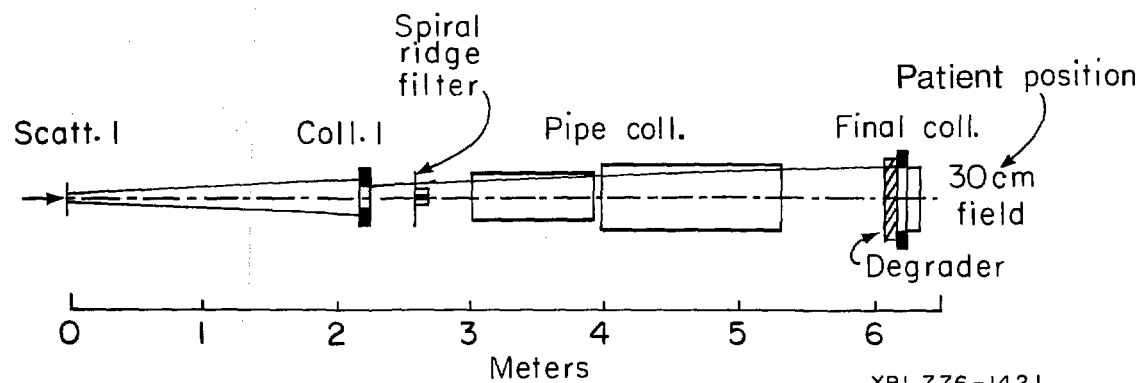
XBL778-1720

FIGURE 1



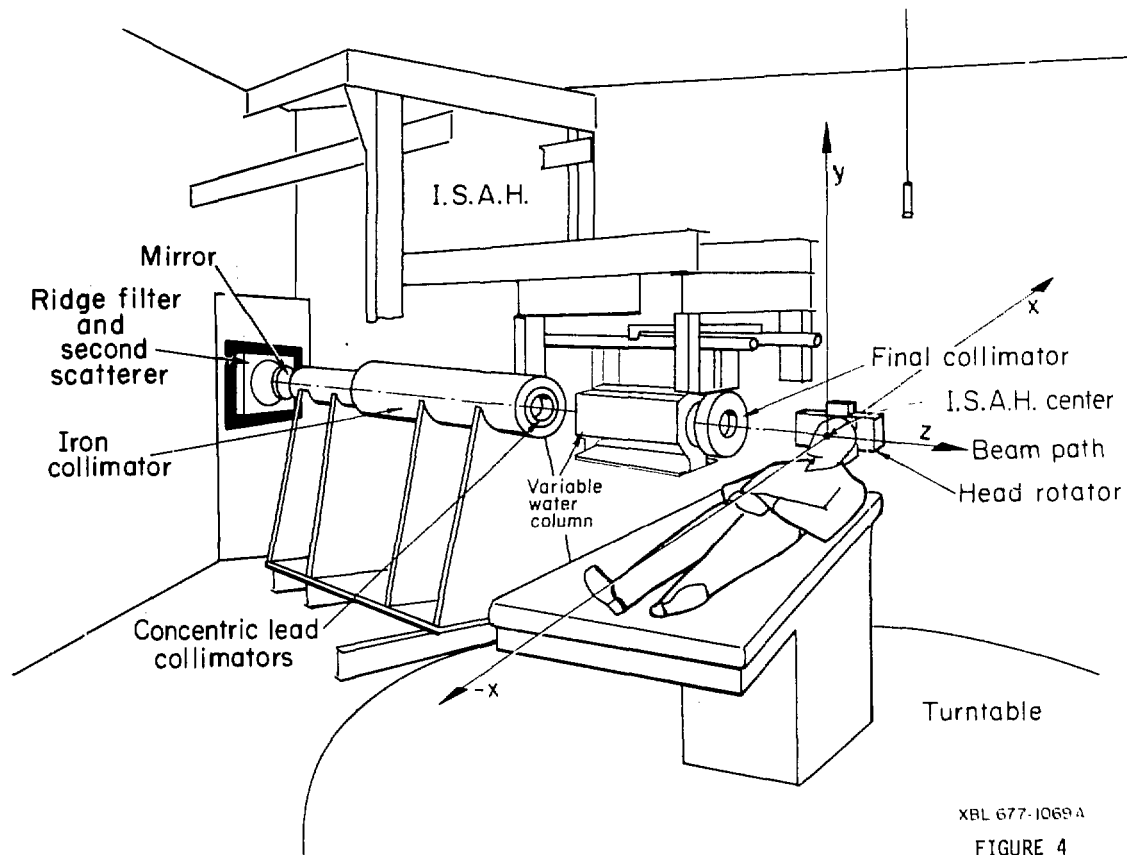
XBL 776-1070

FIGURE 2



XBL 776-1421

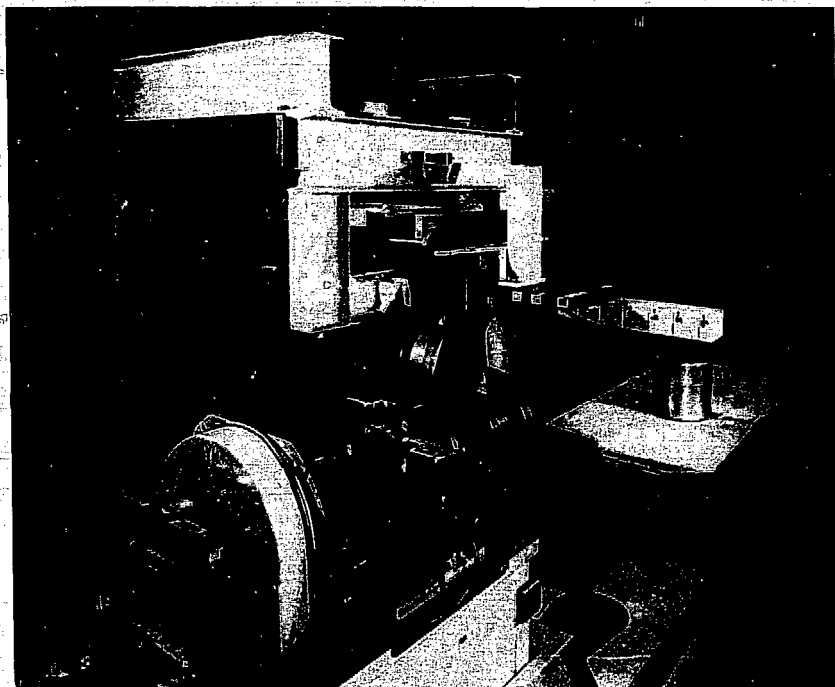
FIGURE 3



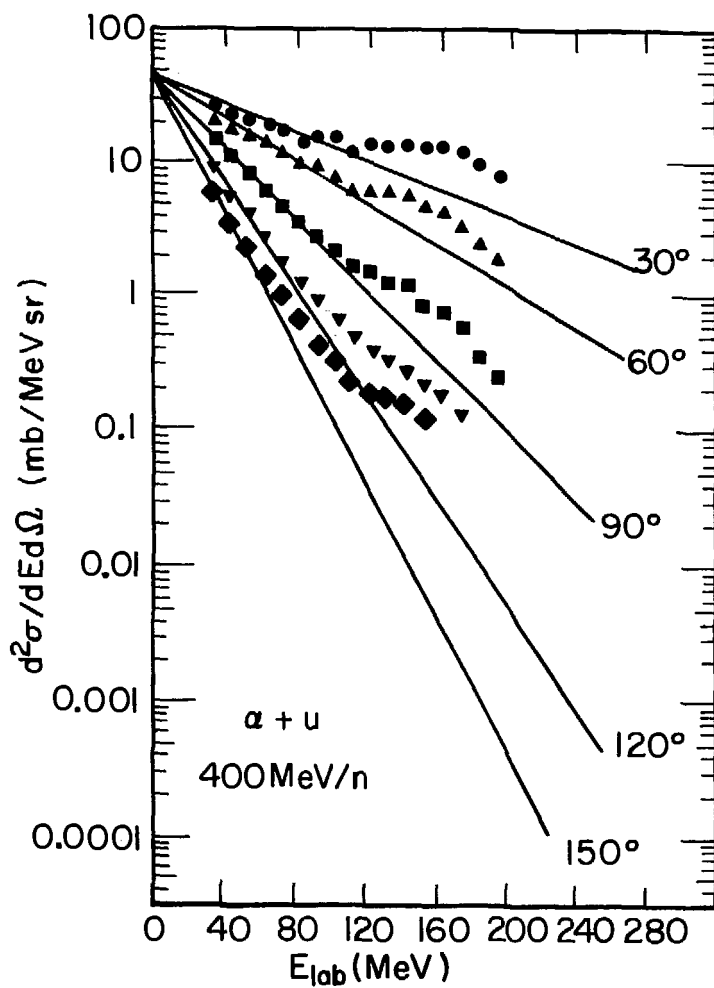


XBB 7610-9342

FIGURE 5

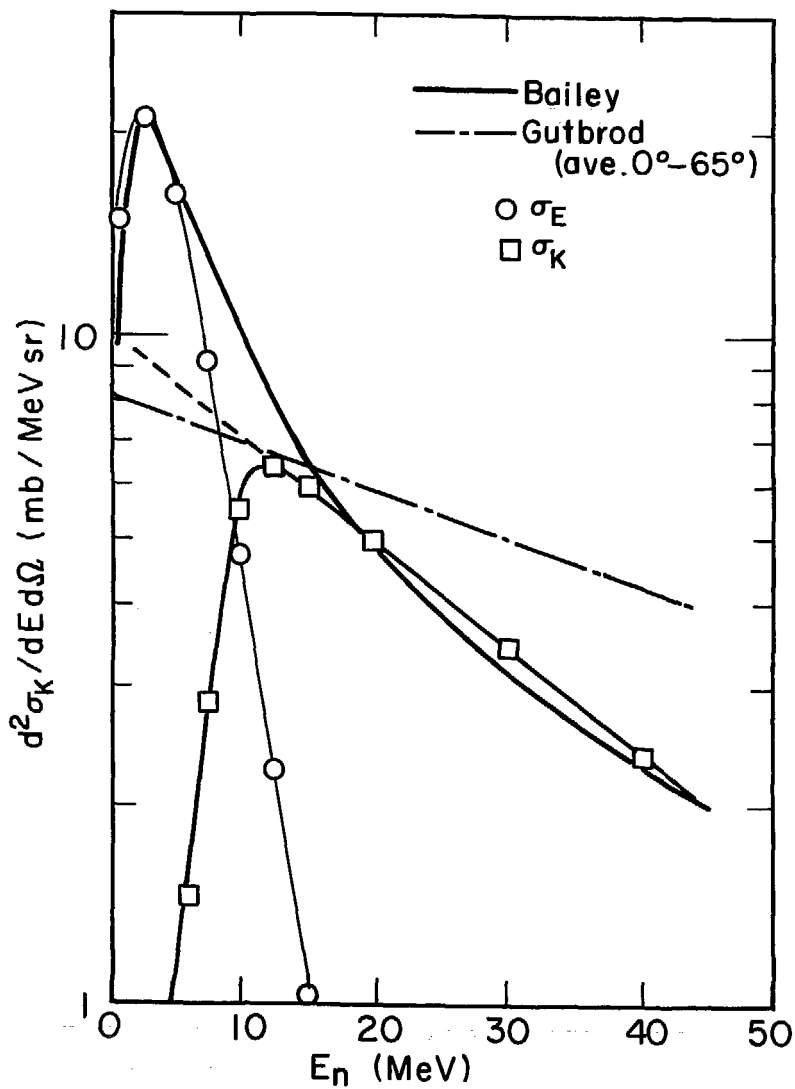


XBB 7610-9343
FIGURE 6



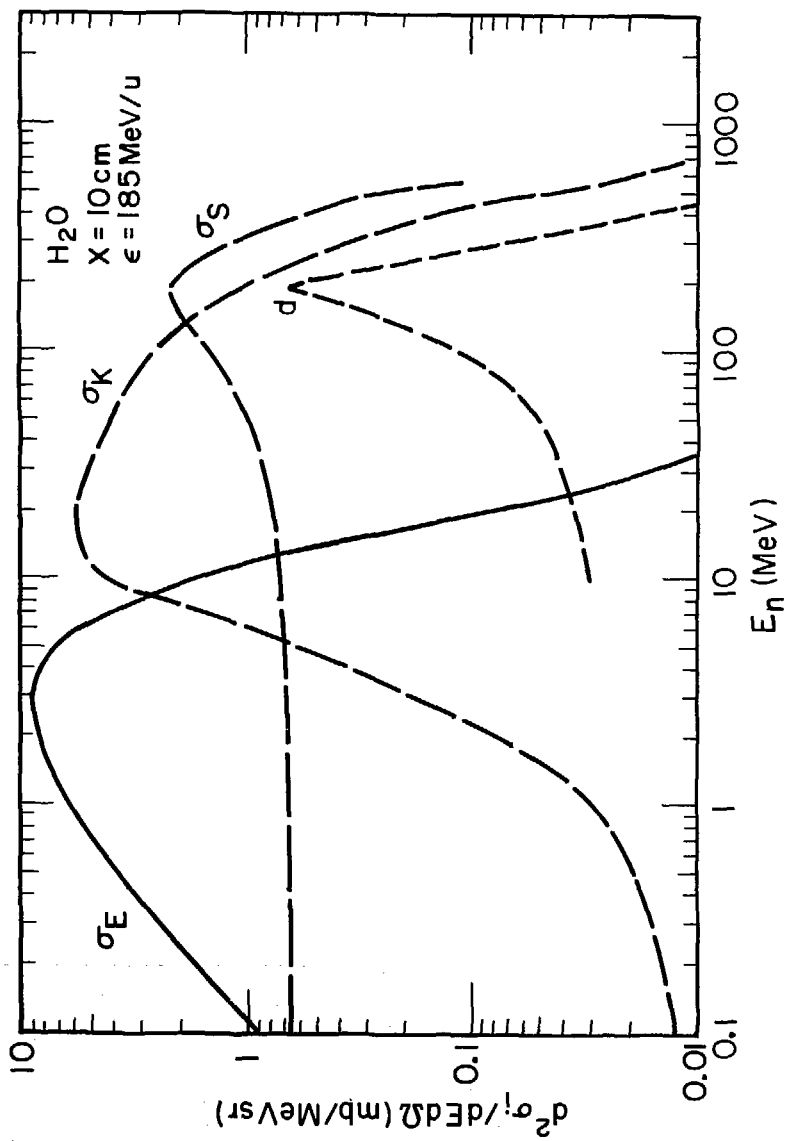
XBL779-3842

FIGURE 7



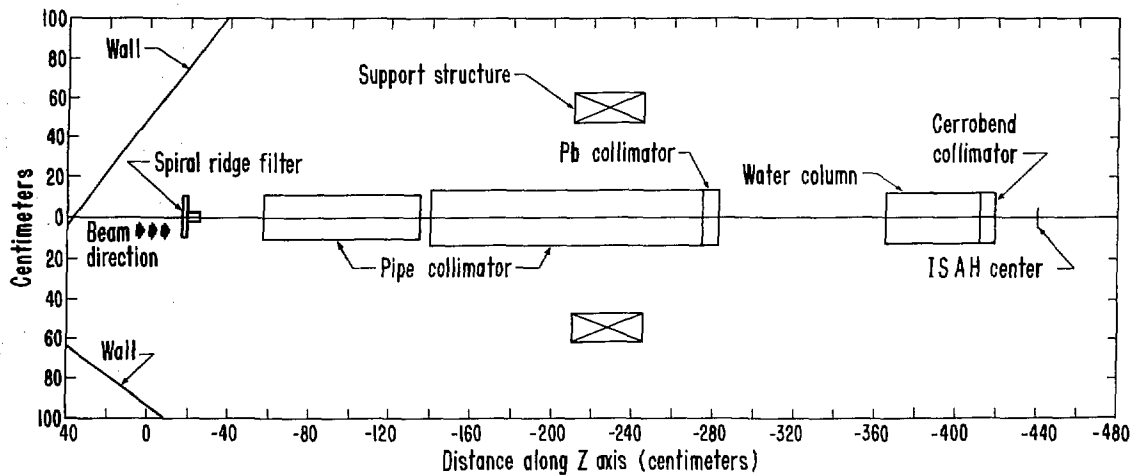
XBL-779-3844

FIGURE 8



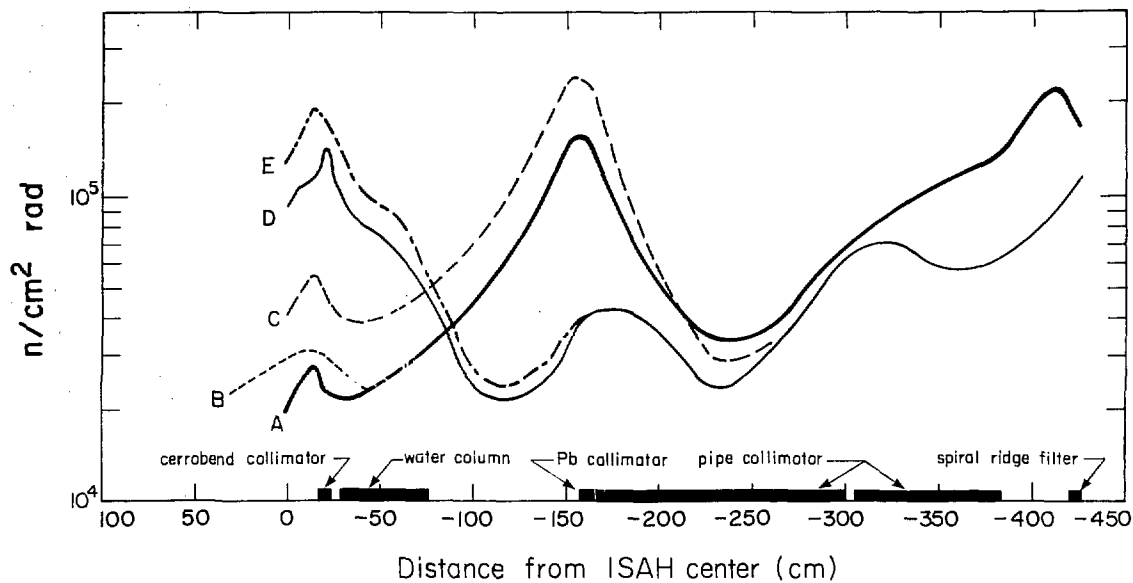
XBL782-2883

FIGURE 9



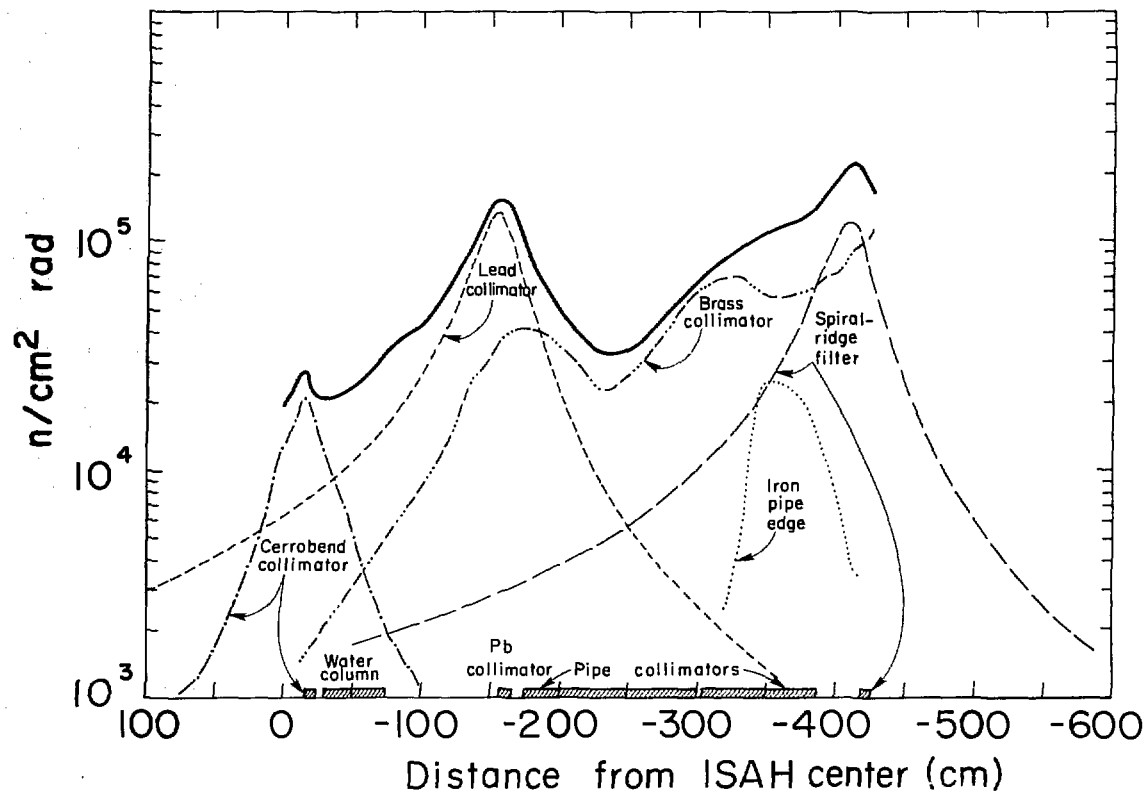
XBL 775-1055

FIGURE 10



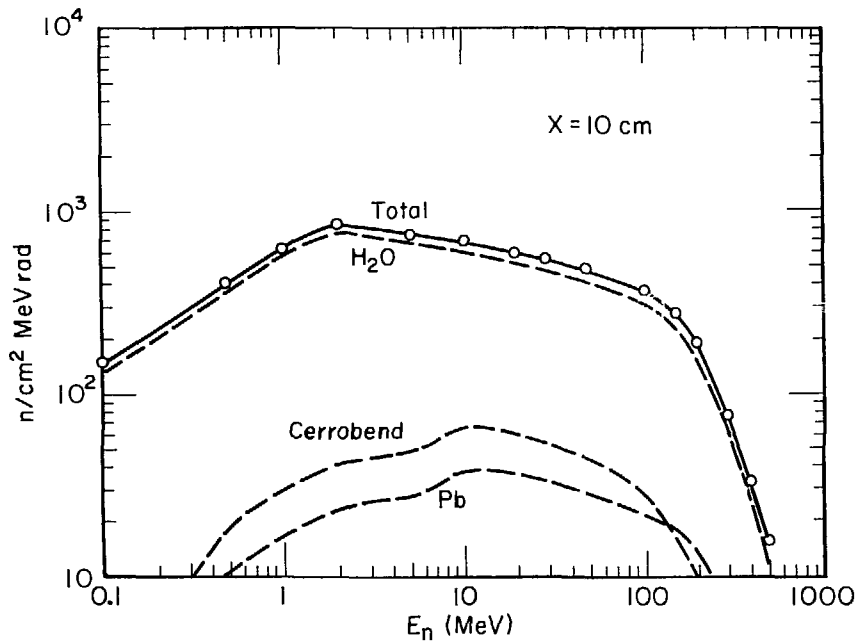
YBL 775-1052

FIGURE 11



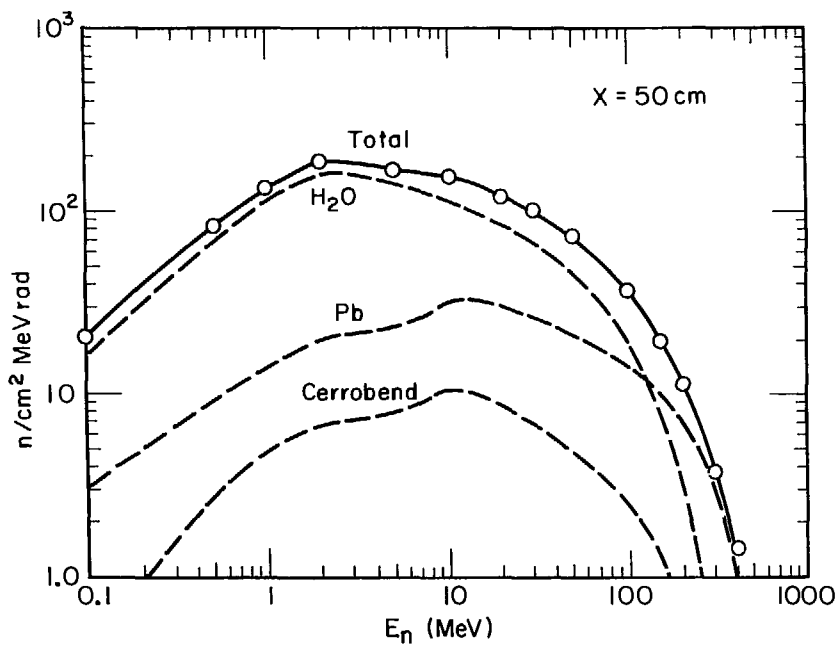
XBL778-1740

FIGURE 12



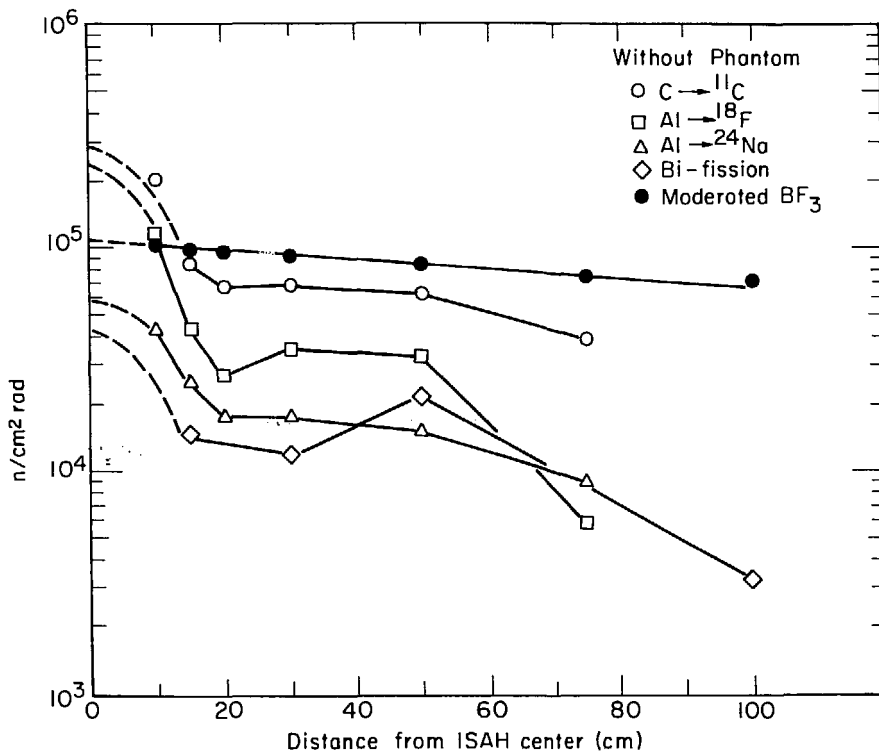
XBL782-2884

FIGURE 13



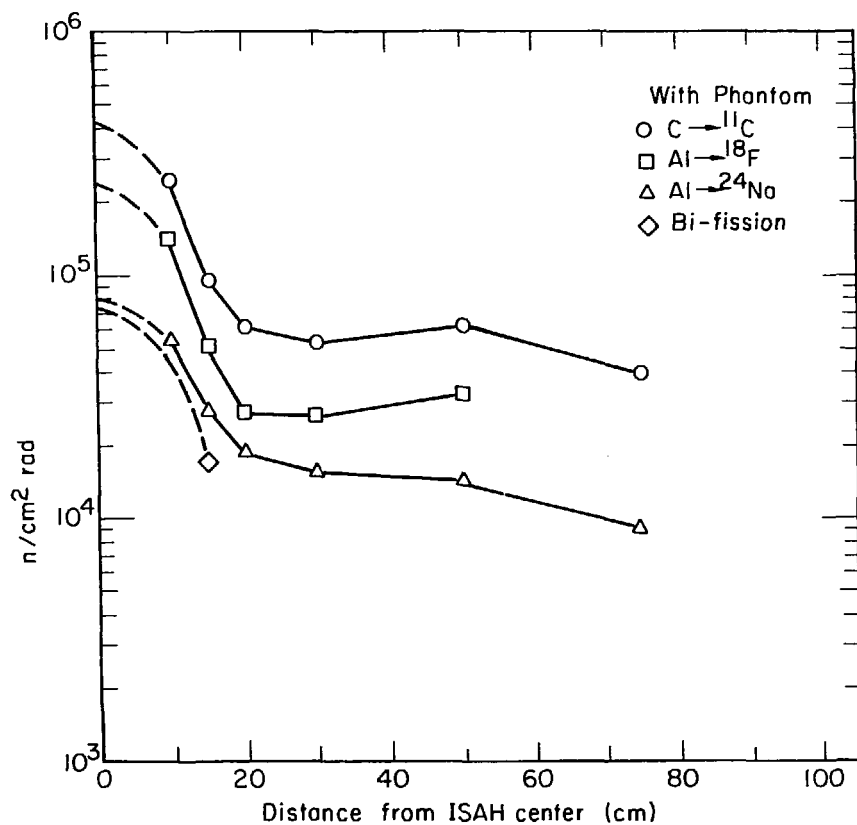
XBL 782-2885

FIGURE 14



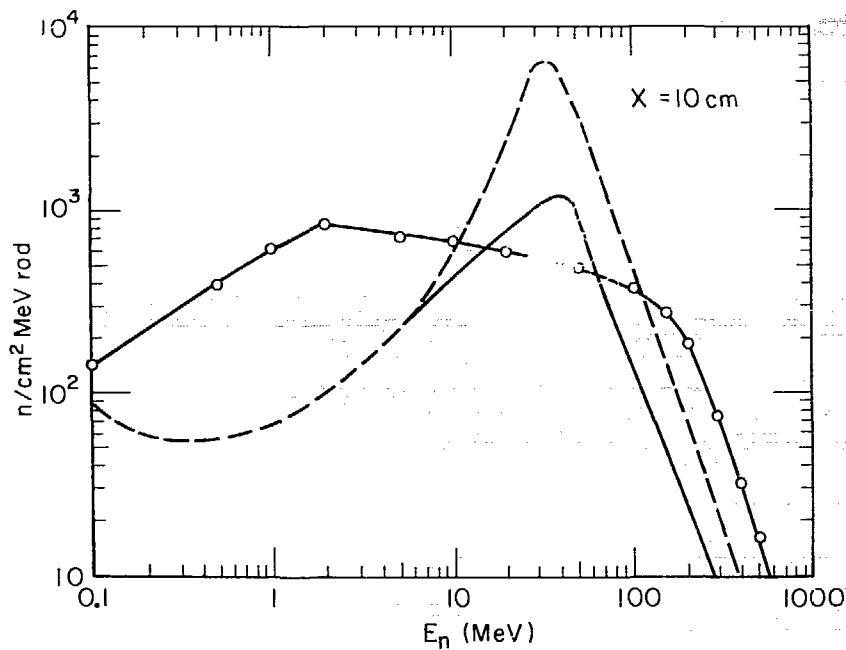
XBL782-2830

FIGURE 15



XBL782-2829

FIGURE 16



XBL782-2886

FIGURE 17